Materials & Design 218 (2022) 110655

Contents lists available at ScienceDirect

Materials & Design

journal homepage: www.elsevier.com/locate/matdes

Pt accelerated coarsening of A15 precipitates in Cr-Si alloys

Anke S. Ulrich [a,*], Alexander J. Knowles [b,c], Valentina Cantatore [d], Ayan Bhowmik [e], Michael T. Wharmby [f], Christine Geers [d], Itai Panas [d], Mathias C. Galetz [a]

[a] High Temperature Materials, DECHEMA-Forschungsinstitut, Theodor-Heuss-Allee 25, 60486 Frankfurt am Main, Germany
[b] School of Metallurgy & Materials, University of Birmingham, Birmingham B15 2TT, UK
[c] Faculty of Engineering, Department of Materials, Imperial College London, Royal School of Mines, Exhibition Road, London SW7 2AZ, UK
[d] Environmental Inorganic Chemistry, Chemistry and Chemical Engineering, Chalmers University of Technology, Kemigården 4, 412 96 Gothenburg, Sweden
[e] Department of Materials Science and Engineering, Indian Institute of Technology Delhi, Hauz Khas, New Delhi 110016, India
[f] DESY Photon Science, Notkestr. 85, 22607 Hamburg, Germany

HIGHLIGHTS

- Pt enhances coarsening of A15 precipitates in Cr-rich Cr-Si-alloys.
- A ternary Cr-rich Cr-Si-Pt phase diagram at 1200°C is proposed.
- Pt causes Cr_{ss}/A15 interface distortion A rim of enhanced Pt concentration destabilizes the Pt-containing A15 precipitates.
- The coarsening mechanism differs between Pt-rich and Pt-lean precipitates.

GRAPHICAL ABSTRACT

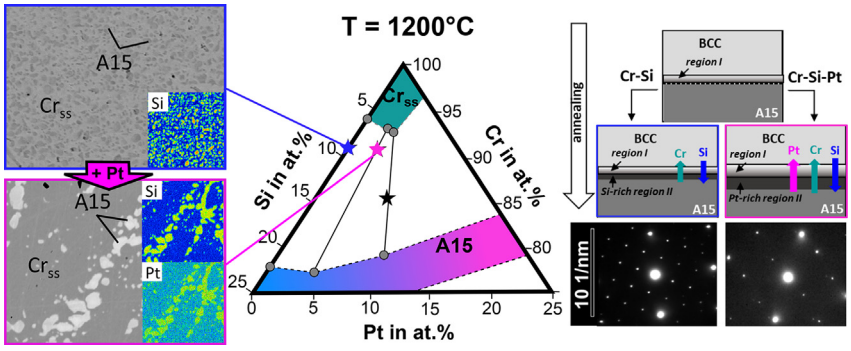

ARTICLE INFO

Article history:
Received 25 November 2021
Revised 4 April 2022
Accepted 10 April 2022
Available online 6 May 2022

Keywords:
High temperature materials
Transition-metal silicides
Coarsening mechanism
Orientation relationship
Density functional theory

ABSTRACT

The effect of alloying Cr-rich Cr-Si alloys with Pt was investigated by a combination of complementary experimental methods and atomic scale modelling. The investigated Cr-Si and Cr-Si-Pt (Cr ⩾86 at.%) alloys developed a two-phase microstructure consisting of Cr solid solution (Cr_{ss}) matrix and strengthened by A15 precipitates during annealing at 1200°C. It was found that additions of 2 at.% Pt increase the coarsening rate by almost five times considering annealing times up to 522 h. Pt was found to change the precipitate matrix orientation relationship, despite its low influence on the Cr_{ss} matrix/A15 precipitate misfit. Through this experimental and modelling approach new insight has been gained into mechanisms of enhanced coarsening by Pt addition. The increased coarsening is principally attributed to a change in interface composition and structure resulting in different thermodynamic stabilities: Pt-containing A15 phase was found to have a broader compositional range if both elements, Pt and Si, are present compared to only Si. Additionally, the Cr_{ss} phase was found to have a higher solubility of Pt and Si over just Si. Both factors additionally facilitated Ostwald ripening.

1. Introduction

During recent years Cr-Si-based alloys comprising solid solutions (Cr_{ss}) reinforced by A15 precipitates, e.g. Cr_3Si, have attracted increased attention as promising light weight materials (ρ_{Cr} = 7.14

* Corresponding author.
E-mail address: silvia.ulrich@dechema.de (A.S. Ulrich).

https://doi.org/10.1016/j.matdes.2022.110655
0264-1275/

$\frac{g}{cm^3}$) for high temperature applications beyond the commonly used Ni-base superalloys (T > 1150°C) [1–4]. Besides high availability as raw material [5], Cr is particularly interesting for the ability to withstand oxidising conditions up to temperatures around 1000°C by Cr_2O_3 formation. This is the basis for why Cr is widely used as an alloying element or in coatings for steels, Ni-base alloys or other commonly used alloys. Alloying Cr with Si greatly improves the oxidation resistance at T > 1000°C due to the formation of SiO_2 alongside Cr_2O_3 [6,5,7,8] and also results in promising wear resistance [9]. More than this, A15 precipitate formation enables microstructural design for strength and hardness that can be optimised and controlled by composition and heat treatment [10–12]. Particularly promising is the high A15 area phase fraction in Cr-Si alloys with Cr $\geqslant$91 at.% which is around 31% of A15 for the binary $Cr_{91}Si_9$ alloy (in at.%) at 1200°C [10]. Ternary and quaternary Cr alloys, such as Cr-Si-Pt and Cr-Si-Ge-Pt, have already been considered to achieve higher A15 precipitation fractions to further increase strength [13].

Major drawbacks to Cr-based alloys are the potential formation of brittle Cr_2N at temperatures above 900°C and a ductile to brittle transition temperature (DBTT) that is above room temperature [14,4,15]. The high DBTT is mainly attributed to impurities such as N, S, or O in Cr_{ss} [16]. A possible approach to lower the DBTT is alloying with scavenger elements to getter the impurities [17].

Pt containing Cr-Si alloys (Cr $\geqslant$89 at.%) are particularly promising as Pt acts as a scavenging element for N, by promoting finely dispersed Cr_3PtN instead of the detrimental Cr_2N scale during high temperature exposure [18,7]. Besides N gettering, Pt is analogous to Si in that both form stable A15 phases with Cr (Cr_3Si, Cr_3Pt), potentially enhancing precipitate design and control. Due to the steeper slope of the $Cr_{ss}/(Cr_{ss}$-A15) solvus curve compared to the binary Cr-Si system, Pt was originally considered to enable more precise adjustment of the A15 phase fraction by heat treatment and thereby solid solution strengthening [19,20]. However, Pt-containing Cr-Si alloys were observed to display a more rapid microstructural coarsening. Since accelerated coarsening is unwanted, the Pt effect on the microstructural evolution has to be investigated in detail with the ultimate goal to understand its cause and be able to introduce countermeasures for onward alloy development.

The focus of the present study on the Cr-Si and Cr-Si-Pt systems is to gain mechanistic insight as to why the microstructures develop so differently. Therefore, the microstructural evolution, orientation relation of matrix/precipitate, lattice parameters, and thermodynamic stabilities of the A15 phases in the binary and ternary systems are investigated. Experimental investigations and 1^{st} principles modelling are used to demonstrate the consistency of results and proposed coarsening mechanism.

2. Experimental procedures

2.1. Sample preparation

Alloys with nominal compositions of $Cr_{91}Si_9$, $Cr_{91}Si_7Pt_2$, and $Cr_{86}Si_8Pt_6$ (in at.%) were melted in a compact arc melter (MAM-1, Edmund Bühler, Germany) on a water-cooled copper mould under a high purity argon atmosphere (the measured compositions are attached in Table A.1 in Appendix A). Ingots of ca. 7 g, 17 mm length, and a diameter of around 10 mm were prepared using Cr pieces (> 99.95 wt.%, Plansee), Si pieces (> 99.999 wt.%, GfE), and Pt pieces (> 99.9 wt.%, Hereaus) were used. Before melting the alloy constituents, a Zr getter was melted twice to capture residual oxygen in the melting chamber. The alloy was remelted five times with turning the ingot over each time. After melting, the ingots were cut into two pieces parallel to the solidification direction (length around 8.5 mm) using wire erosion. The cutting edge was ground up to P320grit (ANSI). For annealing, each half was encapsulated in a quartz glass tube filled with argon which was heated for different times of up to 522 h at 1200°C. Afterwards the samples were quenched in water by simultaneously destroying the quartz glass tube using pliers.

Cross sections of samples after casting and in annealed condition were prepared by mounting the halves in epoxy resin with their cross section face up. They were ground with successively finer SiC papers from P120 to P1000grit (ANSI), polished with 3μm and 1μm diamond suspensions and subsequently relief polished. In all cases the investigated sample cross section is parallel to the solidification direction during casting.

2.2. Sample characterization

The microstructure and the composition were investigated using optical microscopy, a secondary electron microscope (SEM, Philips XL40), and electron probe microanalyser (EPMA, JEOL JXA-8100) with EPMA back scatter images (BSE) and elemental distribution maps taken from each sample as well as quantitative element spot measurements using a wavelength dispersive detector (WDX). An acceleration voltage of 15 kV and a working distance of 11 mm were used. If not stated differently 11 x 11 grid with a step size of 1μm in both *x* and *y* direction was measured from the sample's centre for the quantitative analysis. Image analysis was performed to determine the A15-phase fraction and the particle sizes using *ImageJ 1.51* [21]. For this purpose at least five Si or Pt element maps per sample (*1000x* or *2000x* magnification) were analysed as they offer a higher phase contrast compared to BSE images. The coarsening rate was determined by measuring the average precipitate radius. Therefore, solely secondary precipitates were taken into account and around 80 measurements were taken from each sample.

For transmission electron microscopy (TEM) cylinders with a diameter of ca. 3 mm were cut from annealed ingots perpendicular to the solidification direction using wire erosion. Slices were cut and ground up to a thickness of around 250μm. The specimens were electropolished using a solution of 10 vol.% perchloric acid in methanol, a temperature of −30°C, and a voltage of 18 V. The specimens were examined using double-tilt specimen holders in JEOL 2100F TEM at an accelerating voltage of 200 kV and aperture of 100 nm. Using high-angle annular dark-field images (HAADF) and TEM-energy-dispersive X-ray spectroscopy (TEM-EDX) the microstructure was characterised. To investigate the orientation relationship between matrix and precipitates selected area diffraction patterns (SADP) were recorded. Due to the small size of the precipitates, the orientation of the matrix phase was determined first and subsequently SADP was taken from the interface area of matrix and precipitate.

Prior to the powder X-ray diffraction measurements (PXRD), the ingots were annealed for 100 h at 1200°C and ground using a corundum mortar. After grinding, samples were loaded into 0.8 mm borosilicate glass capillaries and mounted on a capillary spinner. Diffraction data were collected at beamline P02.1 (PETRA III, DESY, Hamburg, Germany) using a wavelength of 0.20698Å with a Perkin Elmer XRD1621 area detector. A sample to detector distance of 1715 mm was used, to maximise two-theta resolution. The beam was centred in the middle of one side of the detector to also maximise two theta range covered whilst still yielding reasonable statistics. Diffraction data were integrated using the DAWN software package [22]. Rietveld Refinements were performed using TOPAS-Academic v6 [23]. Chemical composition information from the EPMA data were included in the refinements as restraints. Details of the restraints applied are given in Table C.3 in Appendix C. Refined values for the elemental composition of each phase, as

well as the overall elemental composition of the sample, and the ratio of the phases present were extracted from each refinement, in addition to lattice parameters and site occupancies.

2.3. Computational methodology

The CASTEP program package [24] within the Material Studios framework [25] was utilized and the PBE GGA functional [26] was employed for all the spin polarized calculations. Core electrons were described by on-the-fly ultrasoft pseudopotentials [27] with 517 eV cut-off energy together with Koelling-Harmon [28] treatment for relativistic effects. All the structures were fully optimised using the Broyden-Fletcher-Goldfarb-Shanno (BFGS) algorithm with the following set of convergence criteria: 10–5 eV/atom for the energy, 0.03 eV/Å for the maximum force, 0.05GPa for the maximum stress, and 0.001Å for the maximum displacement. Employing the Monkhorst–Pack scheme [29] the Brillouin zone was sampled with 0.04Å^{-1} k-point separation, corresponding to 6 x 6 x 1 and a 3 x 3 x 5 meshes for the 1 x 1 x 4 and 2 x 2 x 1 supercells, respectively.

In order to build the empirical foundation for the proposed understanding, supersaturated Cr-Si alloys with six different nominal molar ratios $n_{Si}/(n_{Si}+n_{Cr})$ being 7% Si, 8% Si, 9% Si, 10% Si, 15% Si, and 25% Si, were produced in conjunction with one ternary Cr-Si-Pt alloy with 7% Si and 2% Pt.

3. Experimental results

3.1. Microstructural development during thermal annealing

BSE images of the microstructures are shown in Fig. 1 for the samples in the as-cast condition, after annealing for 100 h at 1200°C, and after annealing for 200 h or 522 h, depending on the composition, at 1200°C. Si and Pt EPMA element maps are included to show the differentiation between the Si- and Pt-rich phase precipitates, and the rather Si-lean matrix. In all cases the observed phases are solely Cr_{ss} matrix and Si- and Pt-rich A15 precipitates which is additionally confirmed by XRD measurements.

After casting, a comparably low area fraction of large A15 precipitates (from around 25μm^2 considering cross sections), so called primary precipitates, is found, principally at grain boundaries. During annealing secondary A15 precipitates (< 5μm^2) form within the former oversaturated Cr_{ss} dendrites, which is described in more detail in [10,12].

Precipitate evolution in the binary $Cr_{91}Si_9$ and ternary $Cr_{91}Si_7Pt_2$ alloy were explored comparing different annealing times at 1200°C. After annealing for 100 h at 1200°C (Fig. 2(a)) a higher fraction of A15 precipitates with sizes below 0.5μm^2 is found for $Cr_{91}Si_9$, hence, the precipitates formed in the binary alloy are rather small compared to the ternary composition. The effect of a longer annealing of 522 h compared to 100 h on the size of the precipitates is shown in Fig. 2(b). After 100 h of annealing (dotted curves) the ternary alloy shows a wider distribution in precipitate size in comparison to the binary alloy. With increasing annealing time the A15 precipitates in both alloys increase in size, however, this effect is much more pronounced for the Pt-containing system and there for large precipitates. To determine the rate of the coarsening process, the mean radius of the secondary precipitates $\langle r\rangle$ is plotted over time. As no secondary precipitates exist at the beginning of annealing, $\langle r_0\rangle$ is set to 0. To investigate the coarsening mechanism, the coarsening rate k is determined. With respect to the LSW theory [30,31] Eqs. 1 and 2 are used to investigate if the coarsening is diffusion (DC) or reaction (RC) controlled.

$$\langle r\rangle^3 - \langle r_0\rangle^3 = k_{DC}\cdot t \tag{1}$$

$$\langle r\rangle^2 - \langle r_0\rangle^2 = k_{RC}\cdot t \tag{2}$$

In both cases a higher coarsening rate is found for the ternary composition in comparison to the binary $Cr_{91}Si_9$ alloy. In addition to the coarsening rates, the coefficient of determination R^2 is given to show the goodness of the respective fit. A higher R^2 value is found the binary composition in the case of assuming diffusion controlled coarsening while a higher R^2 value is obtained for the ternary composition assuming reaction controlled diffusion.

As the increased coarsening was demonstrated upon Pt addition, investigations of phase compositions, phase stabilities, and the interface follow to identify the driving force behind the enhanced microstructural development.

3.2. The stoichiometry of the A15 phase

The compositions of the two phases are measured for the different alloy conditions. The A15 compositions are compared to previous investigations in Fig. 3. The A15 phase has a sub-stoichiometric composition in each of the investigated alloys. Comparative plots of chemical compositions of A15 precipitates after annealing reveal a nearly reproducible Si or Si + Pt content of around 20–22 at.% in the A15 phase which only slightly approaches a maximum with longer annealing times depending on the alloy's composition. Only in the case of the $Cr_{75}Si_{25}$ alloy the A15 phase shows the stoichiometric Si concentration of around 25 at.%. These results suggest a substitution of Si by Pt in the 2(a) position of the A15 phase with the fractions of Pt and Si depend strongly on the Pt concentration in the ternary alloy. The sub-stoichiometric composition is explained by either the formation of vacancies in the 2(a) position, or the occupancy of 2(a) sites additionally by Cr atoms corresponding to $Cr_3(Si_{1-x}Pt_{x-y}Cr_y)$ with y ≈ 0.1–0.2 and x = 0–1.

Synchrotron XRD patterns of both alloys after annealing are shown in Fig. 4 with the corresponding Rietveld Refinements. The XRD measurements confirm that both alloys consist solely of two phases, *bcc* Cr_{ss} with A2 structure ($Im\bar{3}m$) and A15 ($Pm\bar{3}n$). For both phases the determined lattice parameters can be found in Table 1.

Beside the lattice parameters also the site occupancy of the 2(a) site in Cr_{ss} (Cr position) and 2(a) site (Si/Pt position) and 6(c) site (Cr position) in A15 phase are determined and listed in Table 2. For the Rietveld analysis the Cr sites are assumed to be solely occupied by Cr due to the sub-stoichiometric composition of the A15 phase. Si, Pt, and Cr were found to occupy the 2(a) site (respectively B site) of Cr_3B.

3.3. Elemental segregations

Investigating the microstructures in the as-cast condition (compare Fig. 1) it is found, that Pt, in comparison to Si, has a higher tendency to segregate into the Cr_{ss} matrix. This is quantified by the coefficient of segregation:

$$S = \frac{c_{max}}{c_{min}} \tag{3}$$

c_{max} = measured maximum concentration in a phase

c_{min} = measured minimum concentration in the same phase.

S is shown over annealing time in Fig. 5(a). With increasing annealing time, S highly decreases in the case of Pt while for Si it is almost constant in the binary alloy and also shows a low decrease in the ternary alloy. Hence, Pt addition causes an increase in interdiffusion.

Additionally, in the large ternary A15 precipitates contrast variation is observed via the backscatter Z-contrast which is still present after 522 h annealing (compare Fig. 1(h)). To confirm that

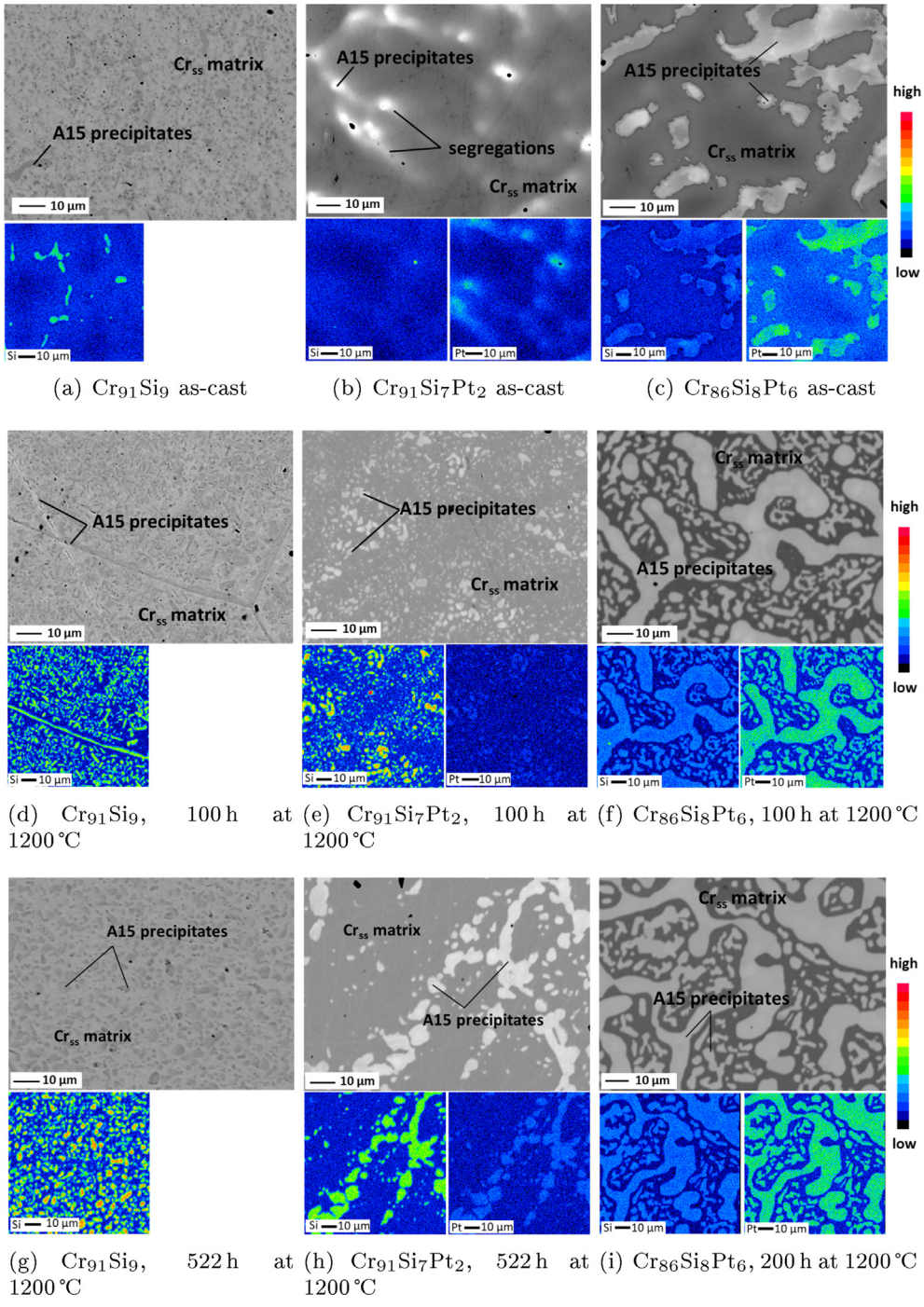

Fig. 1. Cross sections of the three alloys $Cr_{91}Si_9$ ((a), (d), (g)), $Cr_{91}Si_7Pt_2$ ((b), (e), (h)), and $Cr_{86}Si_8Pt_6$ ((c), (f), (i)) in different conditions, as-cast and annealed, showing the phase constitution and qualitative elemental (Si and Pt) distribution maps.

the effect is not an artefact of the measurement, the element concentrations across the A15 phase were measured using EPMA line scans with a step width of 0.3μm. Examples of such scans for both, primary and secondary precipitates, are shown in Fig. 5(b): It is found that especially in the Pt-containing alloy, the Pt concentration in the vicinity of the Cr_{ss}/A15 interface is higher in the A15 phase in comparison to its core while the Si concentration stays almost constant after long annealing times. This is more pronounced in the case of the primary precipitates. In contrast to this, a higher Si concentration is measured in the binary alloy at the Cr_{ss}/A15 interface.

3.4. TEM and orientation relationships in the binary and ternary system

A possible reason for an accelerated microstructural coarsening is a change in the interface orientation and thereby interfacial energy of the A15 precipitates in the Cr_{ss} by Pt alloying. TEM was employed to investigate the orientation relation (OR) between the A2 matrix and A15 precipitates on addition of Pt.

HAADF-STEM images of the microstructures are shown in Figs. 6 and 7 for the binary and the ternary alloy after annealing for 100 h. Again, the A15 phase precipitates can be clearly distinguished from

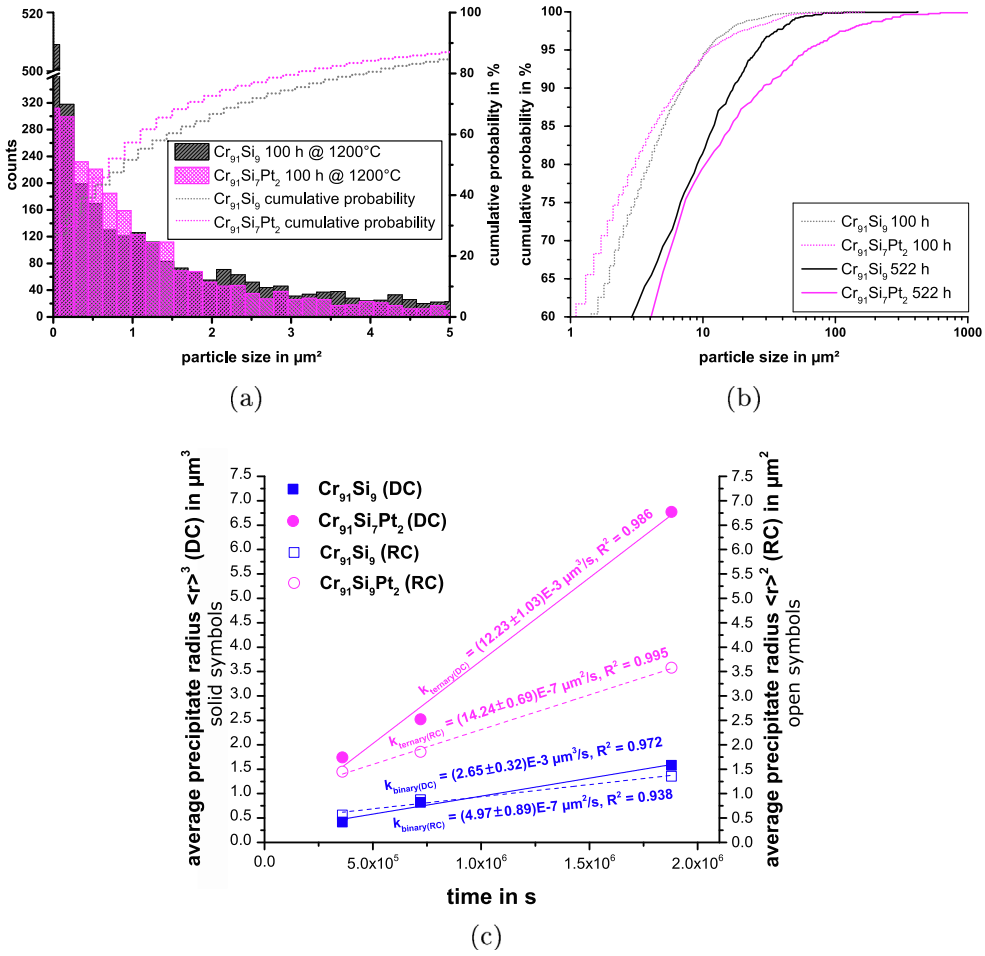

Fig. 2. (a) Histogram of the A15 precipitate size distribution in $Cr_{91}Si_9$ and $Cr_{91}Si_7Pt_2$ after 100 h annealing at 1200°C (magnified for small precipitate sizes). In (b) the cumulative probabilities of particle size are shown for both investigated alloys after 100 h and 522 h annealing at 1200°C; 100% refers to the total area fraction of the A15 precipitates. Additionally, the evolution of $< r >$ over time is shown in Figure (c) and the coarsening rates for both alloys are given as well as R^2.

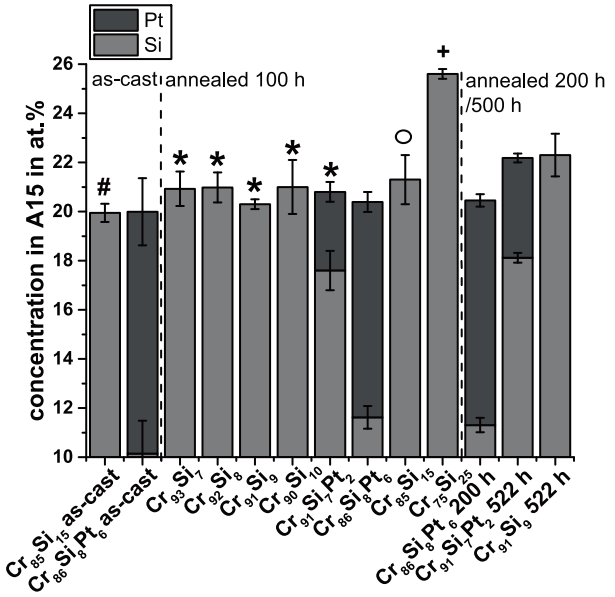

Fig. 3. Concentration of the A15 phase former Si and Pt over alloy composition and heat treatment. The results obtained in this work are compared to other previous studies #[32], o[33], +[6], and *[10]. In all cases a sub-stoichiometric composition of the A15 phase is found except for the pure A15 phase alloy ($Cr_{75}Si_{25}$ in at.%).

the surrounding Cr_{ss} phase by atomic contrast or by Si and Pt element maps (not shown here). A series of SADPs are taken from each investigated alloy from which five areas per sample were fully analysed. The results show that the precipitates and the matrix have a distinct OR that changes with Pt. Selected SADPs with indexed schematics are added to Fig. 6 and 7. Additional SADPs taken from other matrix/precipitate interfaces confirm the distinct ORs, provided in Appendix B. For the determination of the OR only the secondary precipitates (area $\leqslant 5\mu m^2$), which form during annealing, are considered. The identified parallel zone axes obtained from either phase are added to the shown images. The viewing direction along the zone axis of the Cr_{ss} phase is first determined by tilting the specimen along the Kikuchi band and, using the same tilt, collecting combined SADPs from the nearby precipitate-matrix interfacial areas, and the corresponding zone axes of the precipitate-matrix pair identified to obtain the crystallographic parallelisms.

From the overlapping SADPs indexed as $[011]_{A2}$ and $[001]_{A15}$ zone axes of the matrix and the precipitate, respectively, the $\left(0\bar{1}1\right)_{Cr_{ss}}$ and $\left(\bar{1}20\right)_{A15}$ planes are observed to be in coincidence (Fig. 6(c)). Therefore using these crystallographic parallisms, the following OR for the binary $Cr_{91}Si_9$ composition is obtained:

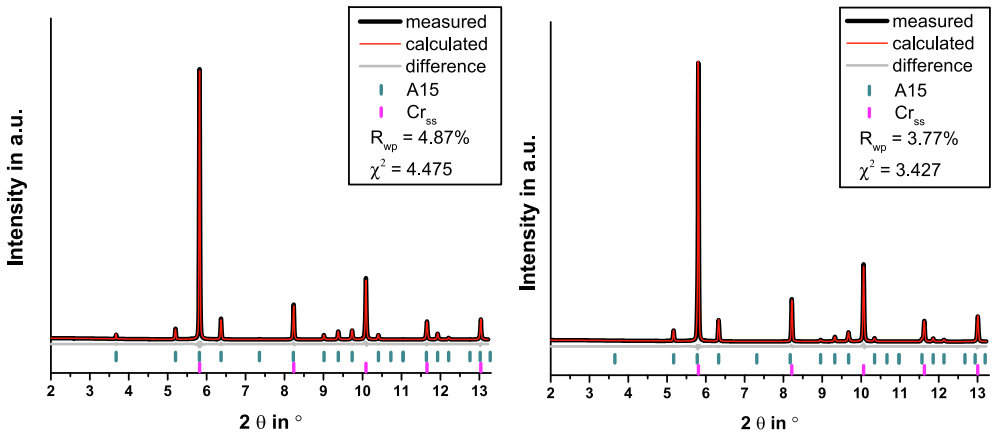

(a) $Cr_{91}Si_9$ (100 h at 1200 °C) (b) $Cr_{91}Si_7Pt_2$ (100 h at 1200 °C)

Fig. 4. Powder XRD pattern of (a) $Cr_{91}Si_9$ and (b) $Cr_{91}Si_7Pt_2$. The Rietveld Refinement is added to the graph as well as the specific diffractions of both found phases. The quality of the refinement is added as well (R-factor and goodness of fit χ^2).

Table 1
Lattice parameters of the A15 and Cr_{ss} phase of the $Cr_{91}Si_9$ and $Cr_{91}Si_7Pt_2$ alloys after annealing for 100 h at 1200°C determined from the diffractions shown in Fig. 4. The accuracy is given with respect to the used monochromatic X-rays and the accuracy of the Rietveld Refinement. Additional information can be found in Appendix C.

alloy	Cr_{ss} in Å	**A15** in Å
$Cr_{91}Si_9$	2.88(2973)	4.56(3576)
$Cr_{91}Si_7$**Pt₂**	2.88(9663)	4.59(1636)

$$\begin{aligned}&[011]_{A2}\|[001]_{A15}\\&\left[0\bar{1}1\right]_{A2}\|\left[\bar{1}\bar{2}0\right]_{A15}\\&[200]_{A2}\|\left[2\bar{1}0\right]_{A15}\end{aligned} \tag{4}$$

In Fig. 7(a) and (c) two sets of SADPs obtained simultaneously from the matrix and precipitate phases of two different regions of interest in the Cr-Si-Pt alloy are displayed, which showed marked differences to the patterns from the binary alloy (Fig. 6) suggestive of a different OR. In Fig. 7(a), $\left[\bar{1}10\right]_{A2}$ zone axis is observed to be parallel to $\left[\bar{3}31\right]_{A15}$, as seen from the overlapped patterns, a key to this composite pattern is shown in Fig. 7(e). Given the difficulty of systematic tilting using such submicron sized precipitates, another set of SAPDs around a different matrix-precipitate combination is obtained and shown in Fig. 7(c). In this case, the corresponding zone axes from the A2 and A15 phases are identified as $[110]_{A2}$ and $[012]_{A15}$ respectively, although, some small angular mismatch is noted between these zone axes. The two sets of zones axes (i.e $\left[\bar{1}10\right]$ and [110] of A2; $\left[\bar{3}31\right]$ and [012] of A15) bear an angular relationship of 60°. Thus the observed parallelisms for $Cr_{91}Si_7Pt_2$ could be expressed as:

$$\begin{aligned}&[110]_{A2}\|[012]_{A15}\\&\left[\bar{1}10\right]_{A2}\|\left[\bar{3}31\right]_{A15}\end{aligned} \tag{5}$$

In the ternary alloy a slight distortion of planes in the A15 diffraction pattern is found by investigating the Cr_{ss}/A15 interface. This is exemplified in Fig. 7(a) with the grey dotted line. To sum up, both alloy systems show different ORs while additionally a change in periodicity of the SADPs is found for the ternary Cr-Si-Pt alloy which was not detected in the binary system.

4. 1*st* Principles modelling

4.1. Modelling considerations

While compositions and sizes of the precipitates change with time during annealing, the modelling of transient phases must connect to the equilibrium characteristics of the relevant thermodynamic phase diagrams. The binary Cr-Si and Cr-Pt phase diagrams are used as boundary conditions for the modelling of the ternary Cr-Si-Pt system. Consistency between calculated and experimental results is obtained for both binary phase diagrams [20,19]. Furthermore, the ability of the A15-structure (A_3B) to accommodate Cr in the A- as well as in the B-position is crucial for the present study. Thus, for the binary systems, this implies reproducing the temperature dependent disproportionation of the alloy into A15 $Cr_3B_{1-x}Cr_x$ and Cr_{ss}(B) phases (B = Si; Pt) from 1^{st} principles. In the ternary system the degree of stability of any $Cr_3Si_{1-x}Pt_{x-y}Cr_y$ precipitate is investigated. The stability of a particular initial ternary precipitate composition is investigated by modellig as well as its spontaneous disproportionation into binary and ternary transients. The focus is on the $Cr_3Si_{0.625}Pt_{0.125}Cr_{0.25}$ composition based on the experimental findings that in the ternary Cr-Si-Pt system the 2(a) sites of the A15-phase are occupied by Si, Pt, and

Table 2
Site occupancy in Cr_{ss} and A15 phase determined by powder XRD and Rietveld Refinement. Samples were annealed for 100 h at 1200°C.

	$Cr_{91}Si_9$		$Cr_{91}Si_7$**Pt₂**		
Cr_{ss}	**Cr**	**Si**	**Cr**	**Si**	**Pt**
2(a)	0.94	0.06	0.94	0.04	0.02
A15	**Cr**	**Si**	**Cr**	**Si**	**Pt**
2(a)	0.12	0.88	0.08	0.76	0.16
6(c)	1.00	0.00	1.00	0.00	0.00

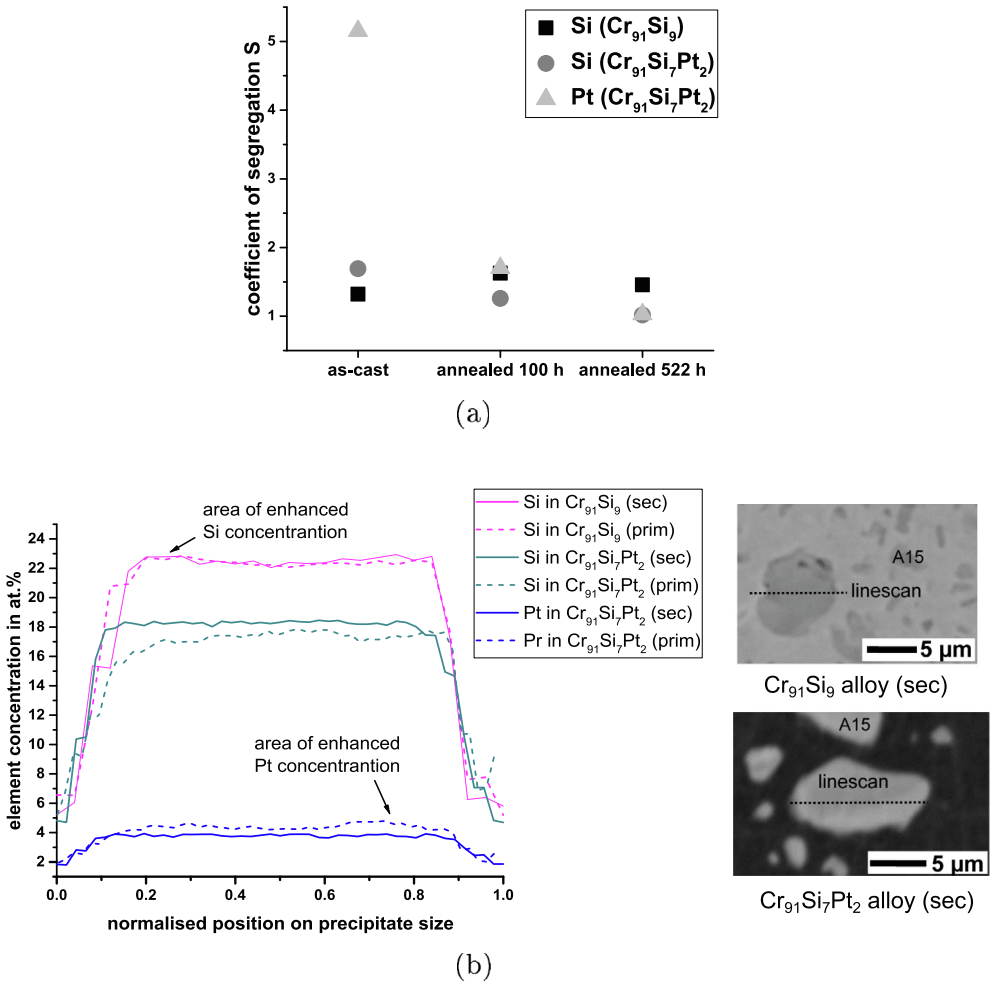

Fig. 5. (a) Segregation coefficient *S* of Si and Pt in Cr_{ss} over annealing time. To demonstrate the tendency for segregation in the A15 phase, selected, normalised EPMA line scans measuring Si and Pt concentrations across A15 precipitates are shown in (b) for the binary and the ternary alloy after annealing for 522 h at 1200°C, respectively. For each composition a line scan across one primary (marked with *prim*) and one secondary (marked with *sec*) precipitate is shown. Corresponding BSE images of the investigated secondary precipitates are added.

Cr atoms resulting in $Cr_3(Si_{0.76}Pt_{0.16}Cr_{0.08})$ with respect to Table 2 and $Cr_3(Si_{0.72}Pt_{0.12}Cr_{0.16})$ with respect to Fig. 3).

Viability of possible disproportionation reactions is addressed by 0 K reaction enthalpy (ΔH) calculations by means of DFT. These results are complemented with configurational entropy contributions (ΔS_{config}) to produce Gibbs free energies of reactions ($\Delta G = \Delta H - T\Delta S_{config}$), thereby comparing predictions at T = 1300 and 1700 K (around 0.82 T_m of the $Cr_{91}Si_9$ alloy). Further information on calculation methodology and configuration entropy assumptions can be found in Appendix D.

4.2. Precipitate transformations

4.2.1. Phase stabilities in binary systems

The phase stabilities of the binary $Cr_3B_xCr_{1-x}$ A15 systems, B being Si or Pt, are investigated by the reaction energies of pure A15 phases (Cr_3Si or Cr_3Pt) with Cr. The energies for the formation of non-stoichiometric, degenerated A15 phases are shown in Fig. 8 (a). The reactions including Cr_3Pt are energetically more favoured in comparison to the reactions in the Cr-Si system. Hence, considering the A15 educt phases a greater deviation from stoichiometry of $Cr_3Pt_{1-x}Cr_x$ than $Cr_3Si_{1-x}Cr_x$ is found which is consistent with the recently reported high stability of the stoichiometric Cr_3Si phase in the binary system [34]. The composition at the outer A15/Cr_{ss} interface changes from A15 $Cr_3B_xCr_{1-x}$ to Cr_{ss}. This is taken into account in Table 3, where variations in B are used to demonstrate the energetically favoured disproportionation of non-stoichiometric A15 phase compositions such as $Cr_3(B_{0.25}Cr_{0.75})$, $Cr_3(B_{0.5}Cr_{0.5})$, and $Cr_3(B_{0.75}Cr_{0.25})$, hence, substitution of around 1.5 at.%, 3 at.% or 4.5 at.% B atom by Cr in the A15 phase. This shows a further enhanced stability of the Si-containing binary A15 precipitates over the Pt-containing A15 precipitates.

4.2.2. Phase stabilities in coupled binary systems

In order to understand the driving force for co-precipitation and precipitate morphology, it becomes relevant to first compare the relative stabilities of the A15 $Cr_3Si_xCr_{1-x}$ and $Cr_3Pt_xCr_{1-x}$ precipitates. This is achieved by coupling the two binary phase diagrams via the transfer of Cr between the two systems. Therefore, reactions between non-stoichiometric binary $Cr_3(B_xCr_{1-x})$ with B is either Pt or Si are considered. It is found that for 3 at.% Si in the Cr_{ss} (considered as $(Cr_3Si_{0.125}Cr_{0.875})$ with A15 crystal structure) and 21 % Pt in A15-phase $(Cr_3Pt_{0.875}Cr_{0.125})$ the formation of Si-rich A15 phase and Pt-rich Cr_{ss} (considered as $(Cr_3Pt_{0.125}Cr_{0.875})$ with A15 crystal structure) is energetically preferred:

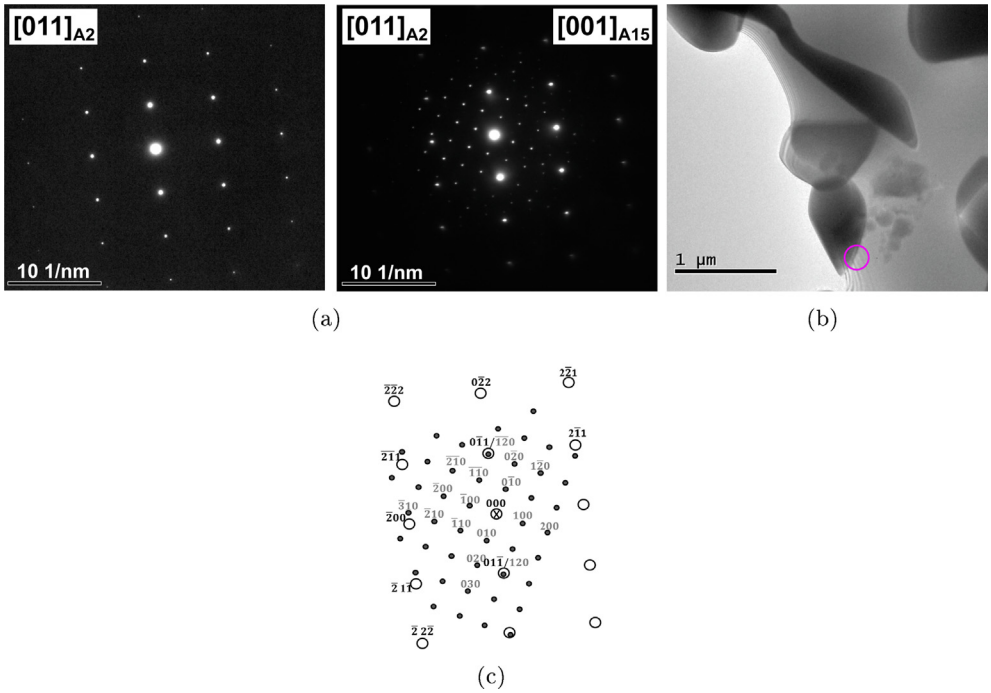

Fig. 6. SADPs of the Cr_{ss} matrix (A2 structure) and the Cr_{ss}/A15 interface of the $Cr_{91}Si_9$ alloy after 100 h at 1200°C annealing are shown in (a). In (b) the corresponding microstructure with the interface from which the SADP was taken (marked) and in (c) an indexed schematic of (a) are shown.

$$\frac{1}{7}Cr_3(Pt_{0.875}Cr_{0.125}) + Cr_3(Si_{0.125}Cr_{0.875}) \rightarrow \frac{1}{7}Cr_3(Si_{0.875}Cr_{0.125}) + Cr_3(Pt_{0.125}Cr_{0.875}); \Delta G = -3.52\frac{kJ}{mol} \quad (6)$$

For this reaction the configuration entropy change is zero, hence, this reaction is insensitive to temperature. For the reaction of other $Cr_3Pt_xCr_{1-x}$ transients ($0.25 \leqslant x \leqslant 0.875$) with 3 at.% Si-containing Cr_{ss} comparable results are found and the formation of $Cr_3Si_{0.875}Cr_{0.125}$ and 3 at.% Pt-containing Cr_{ss} is energetically favourable (see also Table D.6 in Appendix D). Thus, an increased energetic drive is found for any Pt-rich precipitate to react with the Si-rich matrix but it increases with increasing Pt concentration in the A15 phase.

4.2.3. Phase stabilities of the ternaries $Cr_3(Pt_xSi_{1-x})$ and $Cr_3(Si_{1-x}Pt_{x-y}Cr_y)$

To address the stability of ternary precipitates that mix Si, Pt, and Cr in the 2(a) sites within a single A15 precipitate two cases are investigated: Firstly, the $Cr_3(Pt_xSi_{1-x})$ system ($Cr_3(Si_{1-x}Pt_{x-y}Cr_y)$ with y = 0), and secondly, the stability towards disproportionation of a representative precipitate composition $Cr_3(Si_{0.625}Pt_{0.125}Cr_{0.25})$ (compare Table 2). For the first case, a complete miscibility of Cr_3-Si and Cr_3Pt is found above 600 K as shown in Fig. 8(b), hence, a complete miscibility of both A15 phases is found. For the second case, possible fates of $Cr_3(Si_{0.625}Pt_{0.125}Cr_{0.25})$ are explored according to the general disproportion reaction shown in Eq. 7. The energetics for some representative disproportionation reactions can be found in Table 4.

$$Cr_3(Si_{0.625}Pt_{0.125}Cr_{0.25}) \rightarrow \sum_i a_i Cr_3\left[1-x_i^{(Si)} : x_i - y_i^{(Pt)} : y_i^{(Cr)}\right] \quad (7)$$

It is found that three out of five reactions (I, IV, and V in Table 4) are exergonic ($\Delta G < 0\ \frac{kJ}{mol}$), hence, clearly spontaneous at the relevant temperatures while other reactions are endergonic and therefore not spontaneous. However, taking possible subsequent reactions between the products of the endergonic reactions and the surrounding Si-rich Cr_{ss} matrix into account (e.g. from reaction II and III in Table 4) previously considered endergonic disproportionation reactions become energetically favoured as subsequent reactions are exergonic. Such reactions between some transients and Si in the surrounding Cr_{ss} matrix are shown in Reaction 8 and 9.

$$Cr_3Si_{0.5}Pt_{0.5} + \frac{25}{6}Cr_3(Si_{0.125}Cr_{0.875}) \rightarrow 4Cr_3(Pt_{0.125}Cr_{0.875}) + \frac{7}{6}Cr_3Si_{0.875}Cr_{0.125}; \Delta E = -1.08\frac{kJ}{mol} \quad (8)$$

$$Cr_3Si_{0.75}Pt_{0.25} + \frac{13}{6}Cr_3(Si_{0.125}Cr_{0.875}) \rightarrow 2Cr_3(Pt_{0.125}Cr_{0.875}) + \frac{7}{6}Cr_3Si_{0.875}Cr_{0.125}; \Delta E = 0.82\frac{kJ}{mol} \quad (9)$$

By combining Reaction (7)–(9), net reaction energies for mixed ternary $Cr_3(Si_{0.625}Pt_{0.125}Cr_{0.25})$ A15 precipitates reacting with the Cr_{ss}(Si) to form binary $Cr_3(Si_{0.875}Cr_{0.125})$ and Pt-rich Cr_{ss}(Si,Pt) phases are calculated and shown in Table 5. The difference in stability of the products referred to in these tables shows that the formation of $Cr_3[\frac{5}{6};0;\frac{1}{6}]$ (Table 5 ii) is energetically possible but less favoured compared to the formation of the more Si-rich A15 phase $Cr_3[\frac{7}{8};0;\frac{1}{8}]$ (Table 5 i). This is consistent with the enrichment of A15 phase by Si in the binary system over the annealing time as $Cr_3[\frac{5}{6};0;\frac{1}{6}]$ refers to the A15 phase formed after 100 h annealing (around 20.8 at.% Si) and $Cr_3[\frac{7}{8};0;\frac{1}{8}]$ to the A15 phase formed after 500 h annealing with a Si concentration of around 22.0 at.% (compare Fig. 3).

In any case the reaction between the mixed ternary $Cr_3(Si_{0.625}Pt_{0.125}Cr_{0.25})$ phase may take place in contact with the matrix even though the corresponding disproportionation reaction itself is found to be endergonic. The existence of spontaneous exergonic net reactions (compare Table 5) including non-spontaneous reactions (examples shown in Table 4) which in turn react further (Reaction 8 and 9) is understood to control the rates of the solid-state reactions of the ternary composition over time.

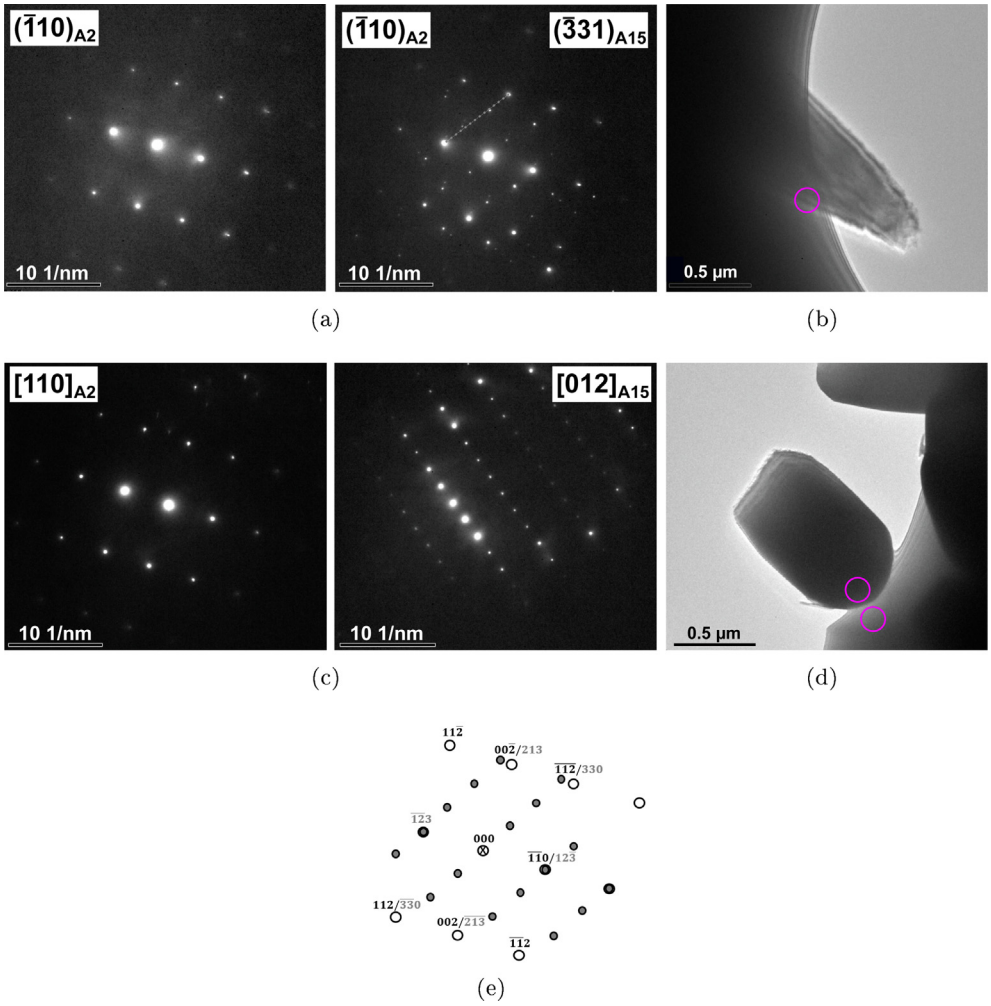

Fig. 7. In (a) and (c) selected SADPs of of $Cr_{91}Si_7Pt_2$ after 100 h at 1200°C annealing are shown. In (b) and (d) the corresponding microstructures of the ternary alloy are shown and the areas from which the SADP were taken are marked. In (a) the pattern is taken from the Cr_{ss} matrix and at the Cr_{ss}/A15 interface, where patterns of both phases are observed. The patterns in (c) are received in the Cr_{ss} matrix and, with the same sample tilt, of the interior of an A15 precipitate in the vicinity. In (e) an indexed schematic of (a) is shown.

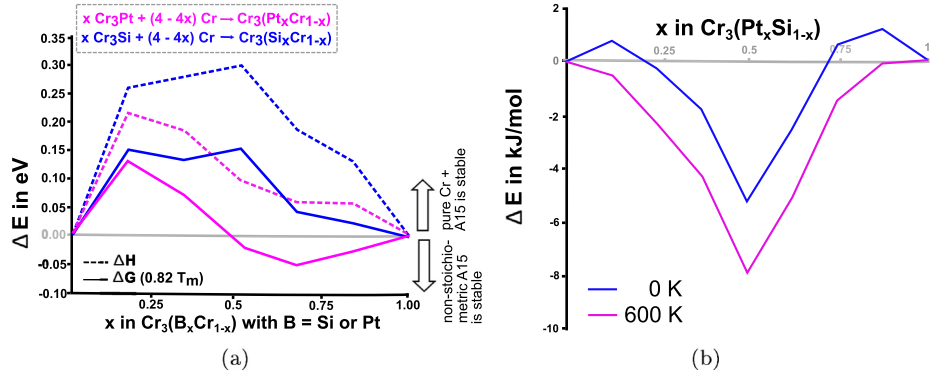

Fig. 8. Stabilities of the (a) non-stoichiometric binary A15 phases and (b) the stoichiometric ternary $Cr_3Pt_xSi_{1-x}$ phase. In (a) both, ΔH at 0 K and ΔG at 0.82 T_m (1700 K) are shown and the corresponding reactions are added. In (b) the stabilities are shown for 0 K and 600 K, the latter referring to the lowest temperature at which the mixed A15 phase shows a full stability over the whole composition range.

5. Discussion

In the beginning of annealing at 1200°C, secondary A15 precipitates are found to nucleate within the Cr_{ss} matrix, which is supersaturated in Si and Pt in the as-cast state due to the fast cooling from the melt. With longer annealing times the coarsening is much more pronounced in the presence of Pt in the alloy which can be seen from Figs. 1 and 2. The ageing of the binary secondary precipitates follows the LSW theory and therefore the conventional Ostwald ripening kinetics. Possible reasons for a Pt induced rate

Table 3
Disproportionation reactions of $Cr_3(Si_xCr_{1-x})$ and $Cr_3(Pt_xCr_{1-x})$ with compositions in the miscibility gap of the binary phase diagrams. $Cr_3(Si_{0.125}Cr_{0.875})$ and $Cr_3(Pt_{0.125}Cr_{0.875})$ represent the Cr_{ss}, $Cr_3(Si_{0.875}Cr_{0.125})$ and $Cr_3(Pt_{0.875}Cr_{0.125})$ represent non-stoichiometric A15 phases. The miscibility gap is found to prevail in case of the Cr-Si system while the endergonic disproportionation energies in the Cr-Pt system show a thermodynamically favoured miscibility of Cr and Pt in the 2(a) site of the A15 structure.

No.	reaction	ΔH in kJ/mol	ΔG at 1300 K in kJ/mol	ΔG at 1700 K in kJ/mol
I	$Cr_3(Si_{0.25}Cr_{0.75}) \rightarrow \frac{1}{6}\,Cr_3(Si_{0.875}Cr_{0.125}) + \frac{5}{6}\,Cr_3(Si_{0.125}Cr_{0.875})$	−21.45	−20.51	−20.22
II	$Cr_3(Si_{0.5}Cr_{0.5}) \rightarrow \frac{1}{2}\,Cr_3(Si_{0.875}Cr_{0.125}) + \frac{1}{2}\,Cr_3(Si_{0.125}Cr_{0.875})$	−20.77	−19.83	−19.55
III	$Cr_3(Si_{0.75}Cr_{0.25}) \rightarrow \frac{5}{6}\,Cr_3(Si_{0.875}Cr_{0.125}) + \frac{1}{6}\,Cr_3(Si_{0.125}Cr_{0.875})$	−7.02	−6.09	−5.80
IV	$Cr_3(Pt_{0.25}Cr_{0.75}) \rightarrow \frac{1}{6}\,Cr_3(Pt_{0.875}Cr_{0.125}) + \frac{5}{6}\,Cr_3(Pt_{0.125}Cr_{0.875})$	−16.83	−15.89	−15.61
V	$Cr_3(Pt_{0.5}Cr_{0.5}) \rightarrow \frac{1}{2}\,Cr_3(Pt_{0.875}Cr_{0.125}) + \frac{1}{2}\,Cr_3(Pt_{0.125}Cr_{0.875})$	−6.43	−5.49	−5.21
VI	$Cr_3(Pt_{0.75}Cr_{0.25}) \rightarrow \frac{5}{6}\,Cr_3(Pt_{0.875}Cr_{0.125}) + \frac{1}{6}\,Cr_3(Pt_{0.125}Cr_{0.875})$	−1.04	−0.11	0.18

Table 4
Energetics for some disproportionation reactions of $Cr_3(Si_{0.625}Pt_{0.125}Cr_{0.25})$.

No.	reaction $\mathbf{Cr_3}(Si_{0.625}Pt_{0.125}Cr_{0.25}) \rightleftharpoons \sum_i a_i Cr_3\left[1-x_i : x_i - y_i : y_i\right]$	ΔH in kJ/mol	ΔG at 1300 K in kJ/mol	ΔG at 1700 K in kJ/mol
I	$\frac{24}{35}\,[\frac{7}{8}: 0: \frac{1}{8}] + \frac{4}{35}\,[0: \frac{7}{8}: \frac{1}{8}] + \frac{1}{5}\,[\frac{1}{8}: \frac{1}{8}: \frac{3}{4}]$	−6.81	−3.48	−2.84
II	$\frac{3}{4}\,[\frac{5}{6}: 0: \frac{1}{6}] + \frac{1}{4}\,[0: \frac{1}{2}: \frac{1}{2}]$	−3.65	−0.63	0.30
III	$\frac{3}{4}\,[\frac{5}{6}: 0: \frac{1}{6}] + \frac{1}{8}\,[0: \frac{1}{8}: \frac{7}{8}] + \frac{1}{8}\,[0: \frac{7}{8}: \frac{1}{8}]$	−2.28	0.97	1.97
IV	$\frac{1}{4}\,[\frac{7}{8}: 0: \frac{1}{8}] + \frac{1}{2}\,[\frac{3}{4}: \frac{1}{4}: 0] + \frac{1}{4}\,[\frac{1}{8}: 0: \frac{7}{8}]$	−10.68	−7.85	−6.97
V	$\frac{13}{24}\,[\frac{7}{8}: 0: \frac{1}{8}] + \frac{1}{4}\,[\frac{1}{2}: \frac{1}{2}: 0] + \frac{5}{24}\,[\frac{1}{8}: 0: \frac{7}{8}]$	−10.03	−6.70	−5.67

Table 5
Possible net reactions of A15 phase and surrounding Cr_{ss} including transient states. The labelling refers to $Cr_3\left[1-x_i : x_i - y_i : y_i\right]$.

No.	reaction	ΔH in kJ/mol	ΔG at 1300 K in kJ/mol	ΔG at 1700 K in kJ/mol
i	$Cr_3\left[\frac{5}{8} : \frac{1}{8} : \frac{2}{8}\right] + \frac{5}{6}\,Cr_3\left[\frac{1}{8} : 0 : \frac{7}{8}\right] \rightleftharpoons \frac{5}{6}\,Cr_3\left[\frac{7}{8} : 0 : \frac{1}{8}\right] + Cr_3\left[0 : \frac{1}{8} : \frac{7}{8}\right]$	−10.30	−6.75	−5.65
ii	$Cr_3\left[\frac{5}{8} : \frac{1}{8} : \frac{2}{8}\right] + \frac{7}{8}\,Cr_3\left[\frac{1}{8} : 0 : \frac{7}{8}\right] \rightleftharpoons \frac{3}{4}\,Cr_3\left[\frac{5}{6} : 0 : \frac{1}{6}\right] + Cr_3\left[0 : \frac{1}{8} : \frac{7}{8}\right] + \frac{1}{8}\,Cr_3\left[\frac{7}{8} : 0 : \frac{1}{8}\right]$	−5.36	−2.10	−1.10

change are a different solubility for A15 phase forming elements in the matrix, a change in vacancy concentration, or an energetic change of the matrix/precipitate interface which includes a change in coherency or a change in interface-reaction.

5.1. The Cr-Si-Pt system

All investigated Cr-Si-Pt alloy compositions in this work and in previous investigations [32,33,6,10] show the formation of a two-phase microstructure consisting of Cr_{ss} matrix with A15 phase precipitates. 1st principles calculations are used to gain insight into the precipitation phenomenon by determining the A15 single-phase stability of the precipitates. The binary $Cr_3(Si_xCr_{1-x})$ and $Cr_3(Pt_xCr_{1-x})$ systems as well as the ternary $Cr_3(Pt_xSi_{1-x})$ and $Cr_3(Si_{1-x}Pt_{x-y}Cr_y)$ systems are investigated in the composition ranges of 75 at.% ⩽Cr ⩽100 at.%, 0 at.% ⩽Si ⩽25 at.%, and 0 at.% ⩽Pt ⩽25 at.%. A favourable miscibility of Si and Pt in the A15 2(a) position resulting in $Cr_3(Pt_xSi_{1-x})$ (compare Fig. 8(b)) is found. Hence, a stable A15 single-phase region connects both binary A15 phases at 1200°C. Based on the experimental and calculated results a schematic Cr-Si-Pt ternary phase diagram is proposed in Fig. 9. The phase fields of Cr_{ss} and A15 phase are schematically shown with respect to phase compositions measured using EPMA.

With respect to this phase diagram all ternary alloys show a tendency for lower A15-phase former concentrations (Si + Pt) in the A15 phase in comparison to the binary compositions. Considering the matrix composition, the total solubility limit of A15 stabilising elements in Cr_{ss} is higher for the ternary alloy compared to the binary. Possible reasons for this are an increase in entropy by adding Pt to the Cr-Si system or a decrease in the enthalpy of mixing. An increased solubility limit c_0 in the solid solution also increases the coarsening rate k. This is expressed by [35]:

$$k \propto D \cdot \gamma_{Ph} \cdot c_0 \tag{10}$$

c_0 = solubility of Si and Pt in Cr_{ss}
γ_{Ph} = specific enthalpy of the interface.
D = diffusion constant.

Following this correlation, increasing c_0 by around 14% in the case of substituting Si by Pt (determined for $Cr_{86}Si_8Pt_6$) should also increase the coarsening rate by about 14%. However, as found by comparing the coarsening rates in Fig. 2(c), Pt increases the microstructural ripening by around three (k_{RC}) or even five (k_{DC}) times. Hence, the increase in solubility limit cannot solely explain the effect of Pt addition on the microstructure ageing.

For completeness it has to be mentioned that the diffusion coefficient of A15 phase former in Cr_{ss} might change by Pt addition which affects the coarsening rate as well. Unfortunately, no data exist on diffusion coefficients of Si and Pt in Cr_{ss}. However, as the matrix phase mainly consists of Cr and the difference in atomic radii of the other elements Si and Pt (Si: 124 pm, Pt: 139 pm [36]) is rather low, small differences in diffusion coefficients between the binary and the ternary alloys are expected.

5.2. Coherence and orientation relationship

The lattice parameters determined for the Cr_{ss} and A15 phases in the binary alloy (see Table 1) are in good agreement with previously determined lattice parameters in different binary alloy systems [2,37,38]. Pt addition especially leads to an increase of the lattice parameter of the A15 phase. The reason is its slightly higher atomic radius. The influence is rather low for the Pt-lean Cr_{ss} but

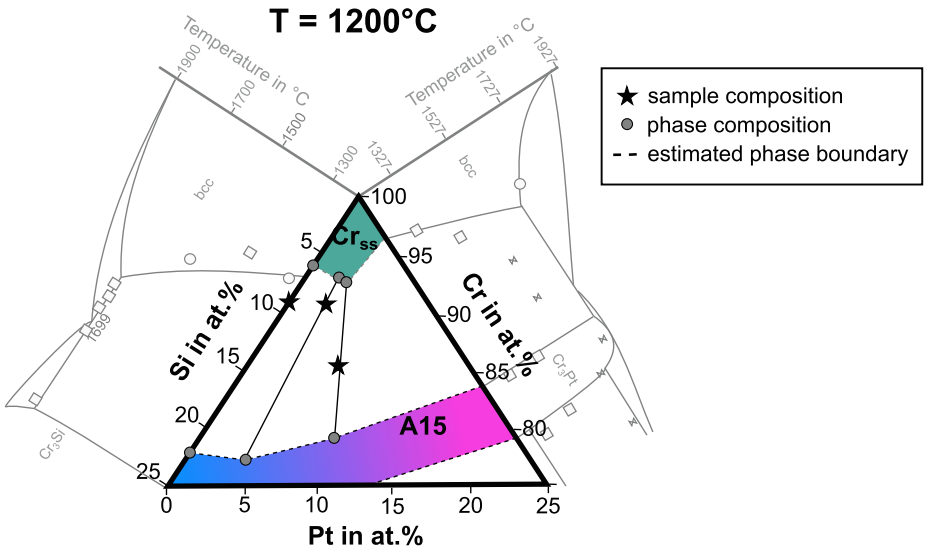

Fig. 9. Schematic isothermal section of the Cr-Si-Pt phase diagram at 1200°C based on EPMA measurements, 1st principles calculations, and the recently assessed binary phase diagrams [20,?].

more pronounced for the A15 phase as Pt is an A15 phase former and it is present in a higher concentration in the A15 phase.

The determined ORs between A2 Cr_{ss} and A15 precipitates are compared to other ORs previously reported for the eutectic Cr_{ss}-Cr_3Si-system in Table 6. Therefore, the matrix relationships in Euqations 4 and 5 are rearranged, to express the ORs in terms of the orthogonal A2 directions assuming them to be the references (x_{ref}, y_{ref}, z_{ref}) frame. Additionally, normalised ORs from various studies are constructed considering the [100], [010], and [001] A2 axes as the orthogonal reference axes x_{ref}, y_{ref}, and z_{ref} for comparison. The OR of the Cr_{ss} matrix and the A15 precipitates determined in this work for the ternary Cr-Si-Pt system (II in Table 6) is found to be comparable to one previously reported OR in eutectic binary Cr-Si alloys produced by directional solidification (III in Table 6) [39]. For the binary alloy, however, the OR obtained in this study is different from [39]. Though apparently, in the binary alloys, the crystallographic relationships might also look different to that obtained in [3] (IV in Table 6) but in fact, they are quite close. With some rearrangement of the crystal orientation, the angular deviation of corresponding A15 directions parallel to the orthogonal reference axes in this study and in [3] could be seen to be quite small. For example the deviations between the $\langle 367\rangle/\langle 647\rangle$ (y_{ref} and z_{ref}) and $\langle \bar{2}10\rangle/\langle \bar{4}30\rangle$ (x_{ref}) directions are 5.4°and 10.3°respectively. So the reported OR for the binary alloy is in close agreement to one previously determined for the eutectic binary $Cr_{84}Si_{16}$ alloy [3]. Hence, in Cr_{ss}-Cr_3Si equilibrium, crystal growth in two phases occurs following either of the two general ORs represented by I or III and II or IV in Table 6. Addition of Pt to Cr-Si system therefore results in a transition from one OR to another, however, the exact transition composition has to be further investigated.

Using the determined ORs (I and II in Table 6) and lattice parameters (Table 1) of the different phases and alloy compositions, the mismatch between Cr_{ss} matrix and A15 precipitates is calculated and listed in Table 7. For the ternary phase the atomic mismatch is not only calculated for the relations found in Eq. 5

Table 6
List of determined ORs depending on the different investigated alloys and their respective normalised form.

alloy	determined OR	normalised OR	reference	No.
$Cr_{91}Si_9$	$[011]_{A2}\|\|[001]_{A15}$ $[0\bar{1}1]_{A2}\|\|[\bar{1}20]_{A15}$ $[200]_{A2}\|\|[2\bar{1}0]_{A15}$	$[100]_{A2}\|\|[2\bar{1}0]_{A15}\|\|x_{Ref}$ $[010]_{A2}\|\|[367]_{A15}\|\|y_{Ref}$ $[001]_{A2}\|\|[\bar{3}67]_{A15}\|\|z_{Ref}$	this work	I
$Cr_{91}Si_7Pt_2$	$(110)_{A2}\|\|(012)_{A15}$ $(\bar{1}10)_{A2}\|\|(\bar{3}31)_{A15}$	$[100]_{A2}\|\|[100]_{A15}\|\|x_{Ref}$ $[010]_{A2}\|\|[031]_{A15}\|\|y_{Ref}$ $[001]_{A2}\|\|[0\bar{1}3]_{A15}\|\|z_{Ref}$	this work	II
$Cr_{85}Si_{15}$	$(111)_{A2}\|\|(001)_{A15}$ $(110)_{A2}\|\|(210)_{A15}$ and $(001)_{A2}\|\|(001)_{A15}$ $(110)_{A2}\|\|(210)_{A15}$	$[100]_{A2}\|\|[3\bar{1}0]_{A15}\|\|x_{Ref}$ $[010]_{A2}\|\|[130]_{A15}\|\|y_{Ref}$ $[001]_{A2}\|\|[001]_{A15}\|\|z_{Ref}$	[39]	III
$Cr_{84}Si_{16}$	$(12\bar{3})_{A2}\|\|(110)_{A15}$ $[111]_{A2}\|\|[100]_{A15}$ and $(0\bar{1}\bar{1})_{A2}\|\|(001)_{A15}$ $(111)_{A2}\|\|(100)_{A15}$	$[100]_{A2}\|\|[3\bar{4}0]_{A15}\|\|x_{Ref}$ $[010]_{A2}\|\|[64\bar{7}]_{A15}\|\|y_{Ref}$ $[001]_{A2}\|\|[647]_{A15}\|\|z_{Ref}$	[3]	IV

Table 7
Calculated mismatches of Cr_{ss} matrix and A15 precipitates. Positive values refer to lower atom distances in the precipitate in comparison to the surrounding matrix and negative values respectively to higher atom distances. The two values given for each OR refer to two 90°-related directions in the respective plane.

OR	$\{011\}_{Cr_{ss}} \parallel \{001\}_{A15}$		$\left\{0\bar{1}1\right\}_{Cr_{ss}} \parallel \left\{\bar{1}20\right\}_{A15}$		$\{200\}_{Cr_{ss}} \parallel \left\{2\bar{1}0\right\}_{A15}$	
Cr-Si	−9.0%	−9.0%	−12.2%	11.3%	−8.9%	11.3%
OR	$\{110\}_{Cr_{ss}} \parallel \{012\}_{A15}$		$\left\{1\bar{1}0\right\}_{Cr_{ss}} \parallel \left\{\bar{3}31\right\}_{A15}$		$\left\{00\bar{2}\right\}_{Cr_{ss}} \parallel \{213\}_{A15}$		$\{110\}_{Cr_{ss}} \parallel \left\{12\bar{3}\right\}_{A15}$	
Cr-Si-Pt	11.0	−11.8	−11.8%	40.8%	−2.7%	−11.8%	5.0%	−2.7%

and Table 6 but also for the parallel planes based on the SADP shown in Fig. 7(a) which are $\{110\}_{Cr_{ss}} \parallel \left\{12\bar{3}\right\}_{A15}$ and $\left\{00\bar{2}\right\}_{Cr_{ss}} \parallel \{213\}_{A15}$.

With respect to Table 7 the mismatches in the ternary system are not markable higher in comparison to the binary system (only the 90°related directions of the Cr-Si-Pt OR $\left\{1\bar{1}0\right\}_{Cr_{ss}} \parallel \left\{\bar{3}31\right\}_{A15}$ stands out). Hence, the huge increase in coarsening by Pt addition cannot be explained solely by the change in coherence.

5.3. Phase stability

1^{st} principles calculations show that, solely considering the binary systems, the sub-stoichiometric Cr-Pt A15 phase ($Cr_3(Pt_xCr_{1-x})$) has a higher stability range compared to the sub-stoichiometric Cr-Si A15 phase (compare Fig. 8(a)). The single A15 phase regime in the Cr-Pt system (c(Pt) = 16.5–20.8 at.%) has a stability range which is twice the A15 stability range of the Cr-Si system (c(Si) = 24.0–26.1 at.%) at 1200°C [20,19], which implies a higher tolerance of intermixing of Pt and Cr in the 2(a) site of the A15 phase. This is fully in line with the fact that a stable $CrPt_3$ phase exists in the binary system but no stable $CrSi_3$ phase [40]. In contrast to this, the stable composition range of Cr_{ss} in the Cr-Si system (c(Si) = 6.5 at.%) at 1200°C is around twice the Cr_{ss} composition range in the Cr-Pt system (c(Pt) = 3.8 at.%). Interestingly, by mixing both systems, the Cr_{ss} regime broadens at least up to c(Si + Pt) = 6.6 at.%.

Based on the results of the DFT calculations, the ternary A15 phase composition $Cr_3(Si_{0.625}Pt_{0.125}Cr_{0.25})$ is found to be metastable at high temperatures. The driving force for spontaneous disproportionation of $Cr_3(Si_{0.625}Pt_{0.125}Cr_{0.25})$ is either given by the exergonic disproportionation reactions itself (compare I, IV, and V in Table 4) or further reactions of disproportionation products with the surrounding Si-rich matrix (compare Table 5). The stabilities of these net reactions also reflect the stability of the Cr-Si A15 phase. Comparing the reactions taking into account a rather Cr-rich binary phase $Cr_3(Si_{0.83}Cr_{0.17})$ ($Cr_3[\frac{5}{6};0;\frac{1}{6}]$) and a rather Cr-lean binary phase $Cr_3(Si_{0.875}Cr_{0.125})$ ($Cr_3[\frac{7}{8};0;\frac{1}{8}]$) it is found, that a higher Cr concentration in the 2(a) site is energetically not preferred.

5.4. Coarsening mechanism

Ostwald ripening is thermodynamically favoured in the binary as well as the ternary system, but its coarsening rate is much a higher for ternary compositions. As already shown for the secondary precipitates in Fig. 2(c) the microstructural coarsening rate of the $Cr_{91}Si_7Pt_2$ alloy in comparison to the $Cr_{91}Si_9$ is around five times higher concerning the average precipitate ratio $< r >^3$. This cannot be explained by the compositional change of the matrix which is also related to diffusion, nor by the change in matrix/precipitate coherence. The effect of vacancies in the A15 phase is assumed to be not decisive. The reason is that (i) the change in composition of the A15 phase is not determined by Pt addition (compare Fig. 3), (ii) the Rietveld Refinements showed very good results even with the presence of vacancies not included, and (iii) 1^{st} principle calculations rather showed a difference in phase stabilities as origin of the enhanced coarsening.

The explanation for the detrimental increase in coarsening is given by the investigation of phase stabilities as well as reaction rates. By looking at the fittings in Fig. 2(c) it is found that for the binary composition the diffusion controlled (DC) fit shows a higher R^2 value while for the ternary composition a reaction controlled (RC) fit has a higher accuracy. This suggests that the Ostwald Ripening in Cr-Si-Pt alloys rather is reaction-controlled or at least that there is a strong contribution of reaction controlled growth.

Additionally, an accelerated coarsening of the primary precipitates in comparison to the secondary precipitates is found, especially in the case of the Cr-Si-Pt composition (see Fig. 2(b)). Both types of precipitates differ in their starting composition. Hence, it becomes evident that any mechanistic understanding of precipitate growth by Ostwald ripening must take also the precipitate composition into account, which was also demonstrated by the energetics of different disproportion reactions (compare Table 4). The coarsening mechanisms and the correlated diffusion processes differ until the composition of the primary precipitates is comparable to the secondary precipitates. Therefore, in the following discussion it is distinguished between Pt-oversaturated (primary) precipitates and precipitates with compositions already close to the equilibrium composition (secondary). A schematic of the coarsening mechanism is visualised in Fig. 10. Included in Fig. 10 is also how the diffusion processes differ for primary and secondary A15 precipitates with respect to the different starting compositions (compare Fig. 3).

5.4.1. Primary precipitates

For binary compositions, the energetic drive to reach equilibrium compositions by disproportionation of Si- or Pt-rich A15 precipitates formed after casting is straight forward (compare also Fig. 8(a)). As found from the annealing experiments, the Cr concentration in A15 phase decreases over time (Fig. 3). It is assumed that Cr is accommodated in the 2(a) position of the A15 crystal structure of the primary precipitates after casting and is partially ejected from the precipitate cores during annealing to approach the equilibrium composition at 1200°C.

For the ternary alloys, the lower solubility of Pt in Cr_{ss} in comparison to Si found for the binary systems at high temperatures [20,19] leads to Si-rich Cr_{ss} dendrite formation from the melt. Increased Pt concentrations are found in the primary precipitates compared to the secondary precipitates that form in the Cr_{ss} during annealing (compare Figs. 1 and 3). The modelling predicts that the reaction between Pt-rich A15 phase and the surrounding Si-rich Cr_{ss}, which is by itself exergonic, is even more pronounced in the case of Pt-oversaturation (compare Reaction 6). The metastable primary precipitates react with the surrounding Si-rich and saturated Cr_{ss} matrix.

With respect to the EPMA concentration measurements (Fig. 5) supported by modelling, the Pt concentration also decreases during annealing in the precipitate core. The DFT calculations showed that there is an energetic drive for the ternary A15 precipitates to transform into a binary $Cr_3(Si_{1-x}Cr_x)$ A15 core with a transient Pt-rich

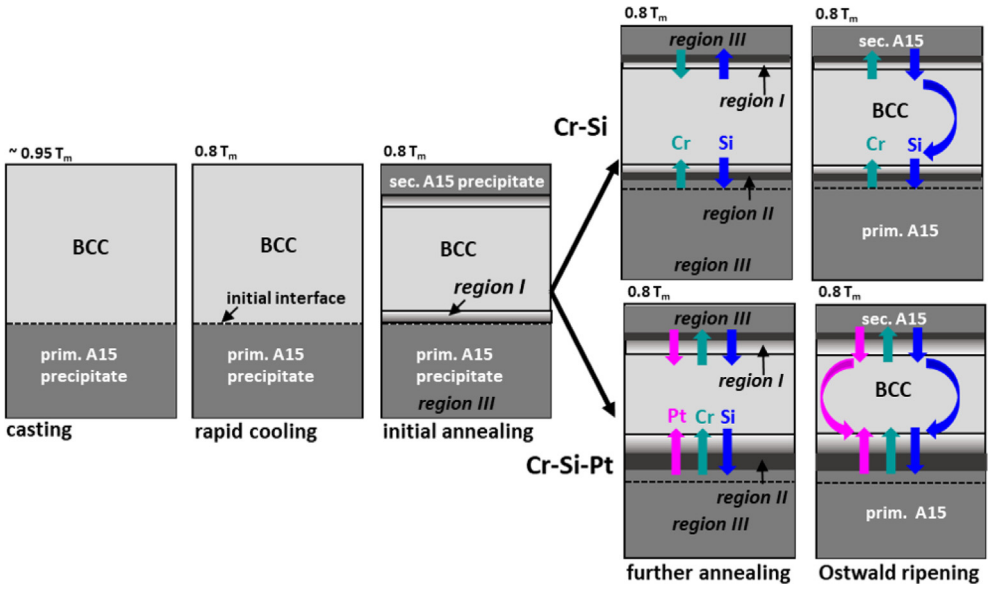

Fig. 10. Schematic of proposed coarsening mechanism showing the evolution of the precipitates from casting towards annealing. The different regions in the A15 phase and the Cr_{ss}/A15 interface are marked (I, II, III). Detailed explanations can be found in the text. Depending on the precipitates (primary or secondary) the diffusing species are shown.

A15 phase area and an outer Pt-rich interfacial region (compare Table 5 and IV and V in Table 4). Based on this it is suggested, that the reaction products segregate locally, resulting in different A15 precipitate regions with slightly different compositions, which are named *region I*, *II*, and *III* in the following and marked in Fig. 10. *Region I* displays the distorted A15/Cr_{ss} interface with increasing Pt- or Si-concentration, *region II* the Pt- or Si-enriched area in the A15 precipitate, and *region III* the inner A15 precipitate area of constant composition. Between all interfaces of these regions and the Cr_{ss} matrix, epitaxy is assumed. The change in crystal structure is attributed to *region I*. Therefore, this region is structurally ill-defined and defect rich.

The higher Si/Pt concentration in *region III* also reflects the higher concentration of Si than of Pt in the A15 phase, considering only the binary systems. This in turn renders the other regions to be enriched in Pt. For the primary precipitates a slightly increased Pt concentration is found close to the A15/Cr_{ss} interface (compare Fig. 5(b)), while this is less pronounced in the case of Si in the binary primary precipitates. Hence, a huge energetic driving force is given by the high Pt concentration in the primary precipitates after casting, resulting in a huge growth of primary precipitates in the first place during annealing (compare Reaction 6). This leads to the formation of net like precipitate structures from former Pt and Si enriched Cr_{ss} areas (compare Fig. 1 and a fast decrease in segregation of A15 phase formers (compare Fig. 5(a)).

5.4.2. Secondary precipitates

Comparable to the primary precipitates also the secondary ternary precipitates have a higher tendency to coarsen in comparison to the binary precipitates. The coarsening rate which refers to the secondary precipitates was found to be three to five times higher (compare Fig. 2(c)). However, in comparison to the immediate coarsening of the Pt-rich primary precipitates directly after casting the driving force is less pronounced for secondary ternary precipitates with lower Pt concentrations. The compositional variations over A15 precipiates (Fig. 5)) and the distorted A15 SADP TEM pattern of secondary precipitates in the vicinity of the Cr_{ss} matrix (compare Fig. 7) support the assumption already made for the primary precipitates of different regions existing in the vicinity of the A15/Cr_{ss} interface. In *region I* and *region II* the composition differs from the A15 precipitate core as well as the lattice parameter. While in the case of the primary precipitates the ternary composition shows an enhanced variation of Pt concentration, this is less pronounced for the secondary precipitates. Hence, the compositional variation between primary and secondary precipitates is higher for ternary alloys in comparison to the binary alloy.

The extension of *region II* can be approximated from the Pt-enrichment in the A15 precipitate boarders showed in Fig. 5(b) which is in the range of 1μm. The shown TEM investigations of the interface refer to even smaller distances directly at the interface of both crystal structure which is referred to as *region I*. Here a distorted A15 crystal structure in comparison to the precipitates core was found which is related to a change in lattice parameter (Fig. 7(c)). However, as this affects the SADP this region consists not only of one atomic layer but has to have a wider extension comparable to *region II*. The greater tolerance of Cr_3Pt to accommodate Si and Cr in the 2(a) position leads to a higher stability of the A15 crystal structure in the distorted Cr_{ss}/A15 interface (*region I*), which gradually changes from A15 (precipitate) to A2 (matrix) structure. Thus, the enhanced compositional stability of the interface region (*region I*) in the case of Cr, Si, and Pt occupying the 2(a) site implies this region to be wider in the ternary composition in comparison to the binary system. Thereby, the dissolution of small ternary precipitates is facilitated, too. As far as the Cr_{ss} remains saturated, the facilitated dissolution process in conjunction with the enhanced structural and compositional tolerance of the interface region of the precipitates serves to enhance the Ostwald ripening.

For completeness it has to be mentioned that the thickness of the distorted interface is assumed to increase by increasing the lattice parameter mismatch and thereby the residual interface energy. This is visible in Table 7 where the highest lattice parameter mismatch (assuming non-distorted crystal structures) is observed for the ternary composition and the $\left(\bar{1}10\right)_{A2} \parallel \left(\bar{3}31\right)_{A15}$ OR. An enhanced mismatch as it is found for the ternary composition is reflected in a distorted interface region (compare SADP in Fig. 7(a)) which in turn is a sign for an increased thickness of *region I*. Hence, it is suggested that the increased mismatch is energetically accommodated by the formation of a distorted interface region which has a higher stability in the ternary system.

6. Conclusion

The effect of alloying of Pt to Cr-Si alloys on the microstructural evolution is shown to cause pronounced A15 precipitate coarsening at 1200°C. Experimental investigations were combined with theoretical 1^{st} principles calculations to investigate this phenomenon. Thereby, the ternary Cr-Si-Pt system was investigated in the Cr-rich corner and new insights were gained into mechanisms influencing the accelerated coarsening behaviour:

- The A15 phase is found to be stable over the whole composition range stretching from the binary Cr_3Si to the binary Cr_3Pt phase at 1200°C. This is not unexpected as Pt and Si occupy the same 2 (a) site in the respective binary A15 phase structures.
- A ternary Cr-Si-Pt phase diagram is proposed for a temperature of 1200°C. A higher concentration of A15 phase forming elements (Si and Pt) of up to 6.6 at.% in Cr_{ss} is reported in the investigated ternary alloys after annealing in comparison to the binary systems.
- The determined precipitate coarsening rates show a rather diffusion controlled Ostwald ripening mechanism for the binary system while the ternary composition rather is reaction controlled.
- The A15 phase shows a sub-stoichiometric composition in the Cr_{ss} - A15 two phase area of the phase diagram. 1^{st} principles calculations and PXRD combined with Rietveld Refinement imply that the 2(a) site in the A15 phase includes besides Si and Pt also Cr. Pt addition enhances the stability of sub-stoichiometric A15 phase leading to added compositional flexibility.
- The increased tolerance in composition of Cr_{ss} and A15 phase by Pt addition enhances the precipitate coarsening rate. Different regions with compositional variations were identified in the A15 precipitates. Starting from the innermost of the precipitate the regions are a rather Pt-poor *region I* A15 precipitate core, a Pt-enriched *region II* outer area, and an interfacial transient *region III* bridging between the A15 and the A2 crystal structure.
- The crystallography between the precipitates and the matrix followed different orientation relationships for the binary and ternary alloy system. The lattice mismatches were observed for the two ORs in the two systems depending on the considered direction, not showing a clear qualitative difference. A distortion of the SADP periodicity was observed in the case of the ternary system, supporting the existence of a chemical tolerant Cr_{ss}/A15 interface region *I*)

To conclude, based on the experimental and theoretical findings, the enhanced tolerance for Cr in the 2(a) site of the A15 phase, and complementarity, the enhanced concentration of A15 phase former in the Cr_{ss}(Si,Pt) matrix, facilitates the Ostwald ripening process by Pt addition.

7. Associated content

CSD 2063086–206308 contains the supplementary crystallographic data for this paper. These data can be obtained free of charge from FIZ Karlsruhe via http://www.ccdc.cam.ac.uk/structures.

Funding

This paper is developed as part of the COMPASsCO2 project, which has received funding from the European Union's Horizon 2020 Research and Innovation Action (RIA) under grant agreement No. 958418. Additionally, it is funded by the Swedish Energy Authority and the Swedish Foundation for Strategic Research project SAFETY (SSF: EM16-0031). This project has received funding from the Chalmers Area of Advance-ENERGY under the funding ID "Light-weight high temperature materials beyond nickel-base alloys". The computations were performed on resources at Chalmers Centre for Computational Science and Engineering (C3SE) provided by the Swedish National Infrastructure for Computing (SNIC). A. Knowles thanks the EUROfusion Research Grant (AWP17-ERG-CCFE/Knowles) and the Royal Academy of Engineering Research Fellowship (RF\201819\18\158) for the financial support. A. S. Ulrich and A. J. Knowles additionally thank the European Feration of Corrosion (EFC) EUROCORR Young Scientist Grant 2019 (EFC-YSG-2019-4) for supporting collaborative TEM investigations.

Data availability

The raw/processed data required to reproduce these findings cannot be shared at this time due to technical or time limitations.

Declaration of Competing Interest

The authors declare that they have no known competing financial interests or personal relationships that could have appeared to influence the work reported in this paper.

Acknowledgements

The authors thank Dr. G. Schmidt from DECHEMA-Forschungsinstitut for EPMA measurements. The authors would also like to express their gratitude to the Plansee Group for providing the chromium raw material used in this work. We acknowledge DESY (Hamburg, Germany), a member of the Helmholtz Association HGF, for the provision of experimental facilities. Parts of this research were carried out at PETRA III using beamline P02.1.

Appendix A. Alloy composition

The measured compositions of the investigated alloys are listed in Table A.1 after casting and annealing. The Cr concentration slightly decreases over time during heat treatments which is attributed to the evaporation of Cr during annealing as Cr develops a high partial pressure at elevated temperatures [41].

Table A.1
Measured compositions of the alloys named with their nominal composition. Results were taken from 121 EPMA point measurements in the sample's centre. The data for $Cr_{91}Si_9$ and $Cr_{91}Si_7Pt_2$ (annealed for 100 h at 1200°C) are based on investigations in [10].

	$Cr_{91}Si_9$		
	c(Cr) in at.%	**c(Si)** in at.%	**c(Pt)** in at.%
as-cast	91.7 ± 0.5	8.2 ± 0.5	-
100 h annealed	90.9 ± 0.3	9.1 ± 0.3	-
522 h annealed	90.0 ±0.7	9.8 ± 0.7	-
	$Cr_{91}Si_7$**Pt$_2$**		
as-cast	91.4 ± 1.6	6.5 ± 0.8	1.9 ± 0.9
100 h annealed	90.9 ± 0.3	6.7 ± 0.2	2.1 ± 0.1
522 h annealed	89.4 ± 0.3	7.8 ± 0.2	2.2 ± 0.1
	$Cr_{86}Si_8$**Pt$_6$**		
as-cast	86.0 ± 0.5	7.5 ± 0.3	6.3 ± 0.2
100 h annealed	85.2 ± 0.4	8.5 ± 0.2	6.0 ± 0.3
200 h annealed	85.4 ± 0.2	8.2 ± 0.1	6.2 ± 0.2

Appendix B. Orientation Relationship

Using the orientation relationships determined in this work and described in Table 6 (I and II), it is straightforward to determine the transformation matrices ${}_{A2}J_{A15,b}$ for the binary (see matrix in Eq. B.1) and ${}_{A2}J_{A15,t}$ for the ternary composition (see matrix in Eq. B.2) which relate the column vectors in the two phases, $\vec{v}_{A2}$ and $\vec{v}_{A15}$.

$$\vec{v}_{A2}={}_{A2}J_{A15,b}\cdot\vec{v}_{A15}=\begin{pmatrix}\frac{2}{\sqrt{5}} & -\frac{1}{\sqrt{5}} & 0\\ \frac{3}{\sqrt{94}} & \frac{6}{\sqrt{94}} & \frac{7}{\sqrt{94}}\\ -\frac{3}{\sqrt{94}} & -\frac{6}{\sqrt{94}} & \frac{7}{\sqrt{94}}\end{pmatrix}\cdot\vec{v}_{A15} \tag{B.1}$$

$$\vec{v}_{A2}={}_{A2}J_{A15,t}\cdot\vec{v}_{A15}=\begin{pmatrix}1 & 0 & 0\\ 0 & \frac{3}{\sqrt{10}} & \frac{1}{\sqrt{10}}\\ 0 & -\frac{1}{\sqrt{10}} & \frac{3}{\sqrt{10}}\end{pmatrix}\cdot\vec{v}_{A15} \tag{B.2}$$

With these matrices an overview of plane parallelism is shown in Table B.2.

To confirm the obtained ORs SADP were taken from around five A15 precipitate/matrix interfaces per alloy composition. It has to be mentioned that all SADP were taken from faceted edges of the precipitate laths every time a crystallographic correspondence with the matrix was assumed. All these interfaces confirm the above written ORs. Further examples are added in Fig. B.1.

Appendix C. Rietveld refinement

Applied restraints used by performing the Rietveld Refinement are summarised in Table C.3. The assumption of a 100% occupancy of the 6(c) site of the A15 phase by Cr is not only validated by the sub-stoichiometric nature of the A15 phase and the goodness of fit (χ) of the Rietveld Refinement but additionally by stability investigations using 1^{st} principles calculations. Using restraints is a valid approach to introduce chemical information, as it biases the refinement towards a particular solution; due to the complexity of the refinements and the number of other free parameters, the restraints do not dictate the final values of refined parameters.

Beside the previously shown lattice parameter and site occupancy, the concentrations of Cr and Si in both phases are also determined using PXRD and Rietveld Refinement. The values are listed in Table C.4 and overall are in good agreement with the EPMA measurements which values are shown in Fig. 3. In comparison to the concentrations determined using EPMA a higher Si concentration was found for the binary system using PXRD while a higher Pt concentration was found in the ternary system compared to the EPMA measurements. This difference is attributed to the different investigated volumes and areas of the samples: The EPMA measurements are always taken from comparable areas in the middle of the samples whereas the PXRD pattern refer to the whole sample composition as the whole sample is ground.

The origin of the large deviations in Table C.4 is there being only five peaks in the diffraction pattern for Cr_{ss}, only one of which is not significantly overlapped with one of the A15 peaks. Hence, a lot of information is extracted from few well defined observations. In the case of the ternary composition, the number of peaks stays the same but the degree of freedom increases for the fit by introducing another parameter, the existence of Pt atoms. An additional factor, which aggravates the determinations lies within the low concentrations of Si and Pt, which is a heavy scatterer. Small changes in the occupancy of Pt have a huge effect on peak intensity (of both phases); small changes in the occupancy of Si have negligible effect on the peak intensity. Thus the precision with which the Si composition of the sample can be determined is always going to be low. As the occupancies are themselves all correlated, since the occupancy of the 2(a) sites in both phases is the sum of the occupancies of all three atoms, the precisions with which the occupancies of the other atoms can be determined are also similarly affected.

In Table C.5 the A15 phase fractions determined using Powder-XRD (PXRD) with Rietveld Refinement are compared to the area phase fractions determined using EPMA measurements on sample cross sections in combination with image analysis. In the latter case an area fraction is measured that is higher in comparison to the volume fraction determined by PXRD and Rietveld Refinement. With around 15% difference in the case of the binary alloy, this is comparable to the differences between area and volume fraction reported for γ'-precipitates in Ni-based superalloys [35].

Table B.2
Parallelism in crystal directions.

A2	A15 $Cr_{91}Si_9$	A15 $Cr_{91}Si_7Pt_2$
1 0 0	2 $\bar{1}$ 0	1 0 0
0 1 0	3 6 7	0 3 1
0 0 1	$\bar{3}$ $\bar{6}$ 7	0 $\bar{1}$ 3
1 1 0	12 2 7	3 3 1
0 1 1	0 0 1	0 1 2
1 0 1	6 10 7	3 $\bar{1}$ 3
$\bar{1}$ 1 0	$\bar{6}$ 10 7	$\bar{3}$ 3 1
0 $\bar{1}$ 1	$\bar{1}$ $\bar{2}$ 0	0 $\bar{2}$ 1
1 0 $\bar{1}$	12 2 $\bar{7}$	3 1 $\bar{3}$
1 1 1	3 1 5	5 3 6
$\bar{1}$ 1 1	$\bar{3}$ 1 5	$\bar{5}$ 3 6
1 $\bar{1}$ 1	1 $\bar{6}$ 0	5 $\bar{6}$ 3
1 1 $\bar{1}$	2 1 0	5 6 $\bar{3}$
0 3 1		0 1 0
0 $\bar{1}$ 3		0 0 1
3 1 $\bar{1}$	1 0 0	
1 1 3		1 0 3
$\bar{5}$ 7 $\bar{7}$	0 1 0	

D.1. Basic modelling considerations

Methodological considerations are validated on the ternary A15 system that mixes Pt and Si in the 2(a) site using 2 x 2 x 1 and 1 x 1 x 4 supercells with the nominal composition $Cr_{24}Si_{8-n}Pt_n$ (n = 0–8). In case of n = 2, 4, 6 the structures are equivalent while for n = 1, 3, 5, 7 they are inequivalent. The overall fine energy scale, the close agreements among nominally equivalent structures, as well as the close agreements among inequivalent structures with the same stoichiometry are taken to reflect the miscibility of Cr_3Pt and Cr_3Si, the accuracy of the used computational approach, and the high configurational entropy of the ternary system (see Fig. D.2).

As a consequence, in all subsequent calculations, no scrambling of Pt, Si or Cr within layers is included, and enthalpy changes of rearrangements among layers are deemed to be negligible. The latter allows for net entropy changes to be estimated from the number of inequivalent permutations of layers, with a factor f for the equipartition in layers stacking directions. Here, $f = 1$ because the stacking direction is decided by that of precipitate growth. For systems binary in the 2(a) position of A15 phase the configuration entropy S^{conf} is

$$S^{conf}=\frac{f\cdot R}{N}ln\left(\frac{N!}{(N-m)!m!}\right) \tag{D.1}$$

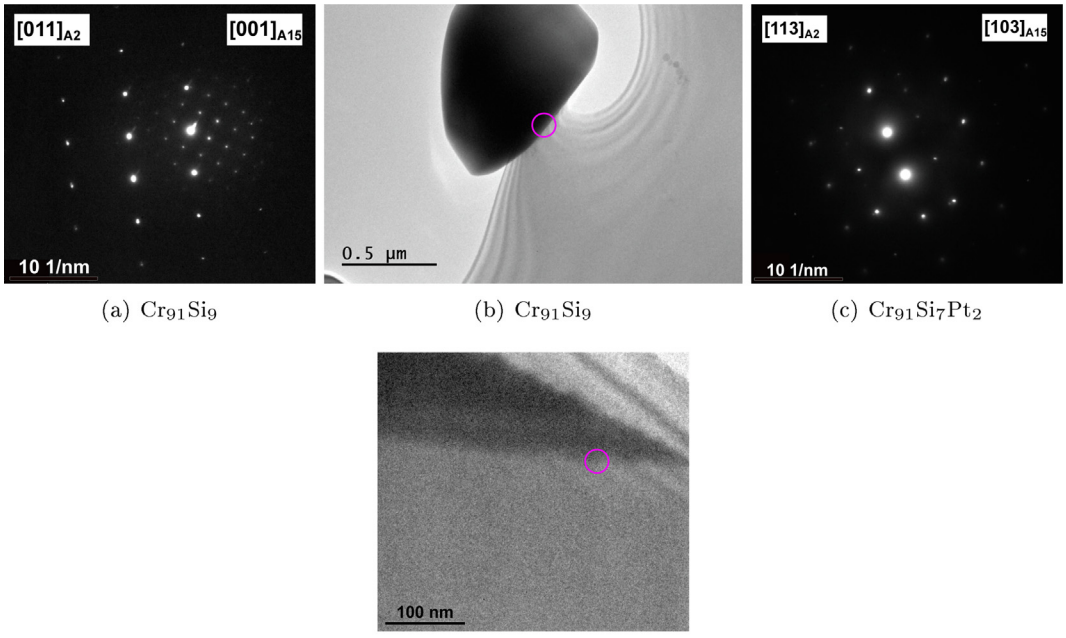

(a) $Cr_{91}Si_9$ (b) $Cr_{91}Si_9$ (c) $Cr_{91}Si_7Pt_2$

(d) $Cr_{91}Si_7Pt_2$

Fig. B.1. Additional SADPs of the Cr_{ss}/A15 interface of the $Cr_{91}Si_9$ ((a) and (b)) and the $Cr_{91}Si_7Pt_2$ ((c) and (d) composition after 100 h annealing at 1200°C taken from the areas marked.

Table C.3
Restraints applied to perform the Rietveld Refinement (alloy compositions, phase fractions and phase compositions). The fraction of each element present in each sample, across all phases, are taken from the EPMA measurements of the respective sample after 522 h annealing (compare Table A.1). For the restraints applied to phase fractions of the two phases present in each refinement a 50% reduced weighting was applied to Cr-Si-Pt refinement.

	Cr-Si alloy	**Cr-Si-Pt alloy**
	alloy composition in wt.%	
Cr	94.25	87.09
Si	5.75	4.14
Pt	-	8.77
	phase fraction in %	
A15 phase	24.85	23.08
Cr_{ss}	75.15	76.92
	elemental fractions in Cr_{ss} and A15 in wt.%	
Si fraction in Cr_{ss}	3.22	2.516
Pt fraction in Cr_{ss}	-	6.92
Si fraction in A15	13.42	9.55
Pt fraction in A15	-	14.95

m = number of inequivalent permutations of the Si_{1-x}, Pt_{x-y} set, and Cr_y in 2(a) position. and for ternary systems ternary in the B position the configuration entropy S^{conf} is

$$S^{conf} = \frac{3R}{N} ln\left(\frac{N!}{(N-m)!\frac{m!}{l!(m-l)!}}\right) \quad (D.2)$$

l = number of inequivalent permutations within the Si_{1-x} and Pt_{x-y} set.

D.2. Phase stabilities in coupled binary systems

Comparable to Reaction 6, reaction energetics for other binary Cr-Pt compositions with $Cr_3(Si_{0.125}Cr_{0.875})$ are shown in Table D.6. It has to be mentioned that the higher Cr concentrations in the Cr-Pt phase refer to the Cr_{ss} phase, hence, changes in configuration entropy have to be considered now.

D.3. Modelling considerations for A15/Cr_{ss} interface

Modelling considerations that enter into the description of the distorted A15/Cr_{ss} interface are:

- In the vicinity of the A15 precipitate the distorted area has the same crystal structure due to epitaxy. Total energies are arrived at by conducting fully optimised supercell calculations that explicitly mix Si or Pt in the non-stoichiometric Cr matrix with A15 crystal structure, i.e. $Cr_{24}XCr_7$ with X = Si, Pt or in the case of pure Cr X = Cr.
- In the vicinity of the Cr_{ss} with A2 crystal structure the crystal structure of the distorted interface changes to A2, too. The total energy is estimated by a two-phase approach, i.e.

$$E_{tot} = 28E_{tot}(Cr(A2)) + E(Cr_3X(A15)) \, with \, X = Si \, or \, Pt. \quad (D.3)$$

The rationales for this formulation are that
- the assumption of local A15 structure offers a realistic distortion of the matrix structure in the vicinity of X,

Table C.4
Measured concentrations in Cr_{ss} and A15 phase after annealing for 100 h at 1200°C.

	$Cr_{91}Si_9$		$Cr_{91}Si_7$**Pt_2**		
	c(Cr) in at.%	**c(Si)** in at.%	**c(Cr)** in at.%	**c(Si)** in at.%	**c(Pt)** in at.%
Cr_{ss}	93.61 ± 1.32	6.39 ± 2.45	93.55 ± 11.94	4.47 ± 17.02	1.99 ± 1.88
A15	78.12 ± 0.08	21.88 ± 0.15	76.89 ± 1.23	19.14 ± 1.68	3.97 ± 0.21

Table C.5
A15 phase fraction after 100 h annealing determined using two different methods. The accuracies of the fit leading to the PXRD and Rietveld Refinement values are given in Fig. 4.

method	$Cr_{91}Si_9$ in %	$Cr_{91}Si_7Pt_2$ in %
EPMA and image analysis after [10]	31.0 ± 1.5	20.9 ± 2.4
PXRD and Rietveld Refinement	25.8 ± 0.5	20.2 ± 4.4

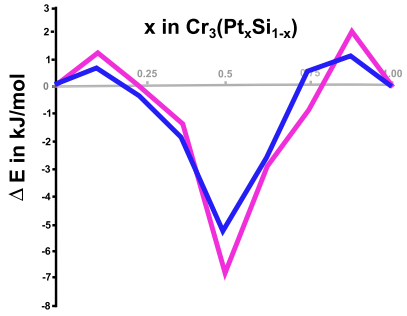

Fig. D.2. Stabilities of $Cr_3Pt_xSi_{1-x}$ showing mutual substitution of Si and Pt in the B position of the A15 structure, virtually independent of 1 x 1 x 4 (pink) or 2 x 2 x 1 (blue) superstructure.

Table D.6
List of couplings of $Cr_3(Pt_xCr_{1-x})$ and $Cr_3(Si_{0.125}Cr_{0.875})$ which lead to the spontaneous formation of $Cr_3(Si_xCr_{1-x})$ A15 phase and $Cr_3(Pt_{0.125}Cr_{0.875})$. $Cr_3(Si_{0.125}Cr_{0.875})$ and $Cr_3(Pt_{0.125}Cr_{0.875})$ both represent non-stoichiometric Cr_{ss}.

reaction	ΔH in kJ/mol	ΔG at 1300 K in kJ/mol	ΔG at 1700 K in kJ/mol
$Cr_3(Pt_{0.25}Cr_{0.75}) + \frac{7}{6}\,Cr_3(Si_{0.125}Cr_{0.875}) \rightarrow \frac{1}{6}\,Cr_3(Si_{0.875}Cr_{0.125}) + 2\,Cr_3(Pt_{0.125}Cr_{0.875})$	−20.94	−20.00	−19.72
$Cr_3(Pt_{0.5}Cr_{0.5}) + \frac{7}{2}\,Cr_3(Si_{0.125}Cr_{0.875}) \rightarrow \frac{1}{2}\,Cr_3(Si_{0.875}Cr_{0.125}) + 4\,Cr_3(Pt_{0.125}Cr_{0.875})$	−18.75	−17.81	−17.53
$Cr_3(Pt_{0.75}Cr_{0.25}) + \frac{35}{6}\,Cr_3(Si_{0.125}Cr_{0.875}) \rightarrow \frac{5}{6}\,Cr_3(Si_{0.875}Cr_{0.125}) + 6\,Cr_3(Pt_{0.125}Cr_{0.875})$	−21.57	−21.08	−20.35

- no influences of lattice mismatches are included, thereby limiting enthalphic stabilities are estimated,
- the inferred near-sightedness renders the configurational entropy of the two model structured of the distorted interfaces equal ($Cr_{24}XCr_7$(A15)/Cr_{28}(A2) and Cr_3X(A15)/Cr_{28}(A2)).

References

[1] K.-M. Chang, B. Bewlay, J. Sutliff, M. Jackson, Cold-crucible directional solidification of refractory metal-silicide eutectics, JOM 44 (6) (1992) 59–63.
[2] J.-A. Sutliff, B.P. Bewlay, H.A. Lipsitt, High-temperature phase equilibria in Cr-Cr_3Si two-phase alloys, Journal of phase equilibria 14 (5) (1993) 583.
[3] H. Bei, E. George, E. Kenik, G. Pharr, Directional solidification and microstructures of near-eutectic Cr–Cr_3si alloys, Acta materialia 51 (20) (2003) 6241–6252.
[4] A.S. Dorcheh, M.C. Galetz, Challenges in developing oxidation-resistant chromium-based alloys for applications above 900C, JOM 68 (11) (2016) 2793–2802.
[5] J.A. Ober, Mineral commodity summaries 2018, Tech. rep., US Geological Survey (2018).
[6] A. Soleimani-Dorcheh, Oxidation-nitridation of chromium at high temperatures and its mitigation by alloying, Ph.D. thesis, RWTH Aachen, Fakultät für Georessourcen und Materialtechnik (2017).
[7] A.S. Ulrich, P. Pfizenmaier, A. Solimani, U. Glatzel, M.C. Galetz, Improving the oxidation resistance of Cr-Si-based alloys by ternary alloying, Corrosion Science 165 (2020) 108376.
[8] M. Poncet, C. Issartel, S. Perrier, H. Buscail, Atmosphere influence on oxidation at high temperature of ni–cr–si model alloys, Oxidation of Metals 96 (1) (2021) 117–127.
[9] J.W. Newkirk, J.A. Hawk, Abrasive wear properties of Cr–Cr_3Si composites, Wear 251 (1–12) (2001) 1361–1371.
[10] A.S. Ulrich, P. Pfizenmaier, A. Solimani, U. Glatzel, M.C. Galetz, Strengthened Cr-Si-base alloys for high temperature applications, International Journal of Refractory Metals and Hard Materials 76 (2018) 72–81.
[11] Y. Aono, T. Omori, R. Kainuma, Microstructure and high-temperature strength in Cr–Si binary alloys, Intermetallics 112 (2019) 106526.
[12] P. Pfizenmaier, A.S. Ulrich, M.C. Galetz, U. Glatzel, Determination of heat treatment parameters by experiments and CALPHAD for precipitate hardening of Cr-alloys with Si, Ge and Mo, Intermetallics 116 (2020) 106636.
[13] A.S. Ulrich, Entwicklung von ausscheidungshärtbaren Cr-Si-Basis-Legierungen für Hochtemperaturanwendungen: Mikrostruktur und Oxidation, Shaker (2020).
[14] Y. Gu, H. Harada, Y. Ro, Chromium and chromium-based alloys: Problems and possibilities for high-temperature service, Jom 56 (9) (2004) 28–33.
[15] F. Müller, B. Gorr, H.-J. Christ, H. Chen, A. Kauffmann, M. Heilmaier, Effect of microalloying with silicon on high temperature oxidation resistance of novel refractory high-entropy alloy Ta-Mo-Cr-Ti-Al, Materials at High Temperatures 35 (1–3) (2018) 168–176.
[16] American society for metals (Ed.), Ductile Chromium and its Alloys, American society for metals, 1957.
[17] A.S. Ulrich, T. Kaiser, E. Ionescu, R. Riedel, M.C. Galetz, Reactive Element Effect Applied by Alloying and SiHfBCN Coating on the Oxidation of Pure Chromium, Oxidation of Metals 92 (3) (2019) 281–302.
[18] M.P. Brady, S.K. Wrobel, T.A. Lograsso, E.A. Payzant, D.T. Hoelzer, J.A. Horton, L. R. Walker, Synthesis of ternary nitrides from intermetallic precursors: modes of nitridation in model Cr_3Pt alloys to form Cr_3PtN antiperovskite and application to other systems, Chemistry of materials 16 (10) (2004) 1984–1990.
[19] J. Preußner, S. Prins, R. Völkl, Z.-K. Liu, U. Glatzel, Determination of phases in the system chromium–platinum (Cr–Pt) and thermodynamic calculations, Materials Science and Engineering: A 510 (2009) 322–327.
[20] S. Cui, I.-H. Jung, Thermodynamic assessments of the Cr-Si and Al-Cr-Si systems, Journal of Alloys and Compounds 708 (2017) 887–902.
[21] C.A. Schneider, W.S. Rasband, K.W. Eliceiri, NIH Image to ImageJ: 25 years of image analysis, Nature methods 9 (7) (2012) 671–675.
[22] J. Filik, A. Ashton, P. Chang, P. Chater, S. Day, M. Drakopoulos, M. Gerring, M. Hart, O. Magdysyuk, S. Michalik, et al., Processing two-dimensional X-ray diffraction and small-angle scattering data in DAWN 2, Journal of applied crystallography 50 (3) (2017) 959–966.
[23] A.A. Coelho, TOPAS and TOPAS-Academic: an optimization program integrating computer algebra and crystallographic objects written in C++, Journal of Applied Crystallography 51 (1) (2018) 210–218.
[24] S.J. Clark, M.D. Segall, C.J. Pickard, P.J. Hasnip, M.I. Probert, K. Refson, M.C. Payne, First principles methods using CASTEP, Zeitschrift für Kristallographie-Crystalline Materials 220 (5–6) (2005) 567–570.
[25] D. Module, Materials Studio 6.0, Accelrys, Inc., San Diego, CA (2010).
[26] J.P. Perdew, K. Burke, M. Ernzerhof, Generalized gradient approximation made simple, Physical review letters 77 (18) (1996) 3865.
[27] D. Vanderbilt, Soft self-consistent pseudopotentials in a generalized eigenvalue formalism, Physical review B 41 (11) (1990) 7892.
[28] D. Koelling, B. Harmon, A technique for relativistic spin-polarised calculations, Journal of Physics C: Solid State Physics 10 (16) (1977) 3107.
[29] H.J. Monkhorst, J.D. Pack, Special points for Brillouin-zone integrations, Physical review B 13 (12) (1976) 5188.
[30] I.M. Lifshitz, V.V. Slyozov, The kinetics of precipitation from supersaturated solid solutions, Journal of physics and chemistry of solids 19 (1–2) (1961) 35–50.
[31] C. Wagner, Theorie der Alterung von Niederschlägen durch Umlösen (Ostwald-Reifung), Zeitschrift für Elektrochemie, Berichte der Bunsengesellschaft für physikalische Chemie 65 (7-8) (1961) 581–591.
[32] A. Soleimani-Dorcheh, M.C. Galetz, Cr-Ge-Si Alloys for High-Temperature Structural Applications: Microstructural Evolution, Metallurgical and Materials Transactions A 45 (3) (2014) 1639–1645.
[33] A. Soleimani-Dorcheh, M. Galetz, Oxidation and nitridation behavior of Cr–Si alloys in air at 1473 K, Oxidation of Metals 84 (1–2) (2015) 73–90.
[34] Y. Pan, D.L. Pu, E.D. Yu, Structural, electronic, mechanical and thermodynamic properties of Cr–Si binary silicides from first-principles investigations, Vacuum 185 (2021) 110024.
[35] R. Bürgel, H.J. Maier, T. Niendorf, Handbuch Hochtemperatur-Werkstofftechnik, 5th Edition., Springer, 2011.
[36] Y. Tarutani, M. Kudo, Atomic radii and lattice parameters of the A15 crystal structure, Journal of the Less Common Metals 55 (2) (1977) 221–229.
[37] M. Jurisch, G. Behr, Growth and perfection of Cr_3Si single crystals, Acta physica Academiae Scientiarum Hungaricae 47 (1) (1979) 201–207.
[38] A. Gokhale, G. Abbaschian, The Cr- Si (Chromium-Silicon) system, Journal of Phase Equilibria 8 (5) (1987) 474–484.
[39] B. Bewlay, J. Sutliff, M. Jackson, K. Chang, Processing, microstructures, and properties of Cr-Cr_3Si, Nb-Nb_3Si, and V-V_3Si eutectics, Material and Manufacturing Process 9 (1) (1994) 89–109.
[40] A. Alsaad, A.A. Ahmad, T.S. Obeidat, Structural, electronic and magnetic properties of the ordered binary FePt, MnPt, and $CrPt_3$ alloys, Heliyon 6 (3) (2020) e03545.
[41] N. Birks, G.H. Meier, F.S. Pettit, Introduction to the high temperature oxidation of metals, Cambridge University Press, 2006.